Article:

Isteri, V., Ohenoja, K., Hanein, T. orcid.org/0000-0002-3009-703X et al. (6 more authors) (2022) Ferritic calcium sulfoaluminate belite cement from metallurgical industry residues and phosphogypsum : clinker production, scale-up, and microstructural characterisation. Cement and Concrete Research, 154. 106715. ISSN 0008-8846

https://doi.org/10.1016/j.cemconres.2022.106715

Cement and Concrete Research 154 (2022) 106715

Contents lists available at ScienceDirect

Cement and Concrete Research

journal homepage: www.elsevier.com/locate/cemconres

Ferritic calcium sulfoaluminate belite cement from metallurgical industry residues and phosphogypsum: Clinker production, scale-up, and microstructural characterisation

Visa Isteri[a], Katja Ohenoja[b], Theodore Hanein[c,d], Hajime Kinoshita[d], Holger Kletti[e], Christiane Rößler[e], Pekka Tanskanen[a], Mirja Illikainen[b], Timo Fabritius[a,*]

[a] Process Metallurgy, Faculty of Technology, PO Box 4300, 90014, University of Oulu, Finland
[b] Fibre and Particle Engineering, Faculty of Technology, PO Box 4300, 90014, University of Oulu, Finland
[c] Manatee Consulting Limited, Sheffield S3 7XL, UK
[d] Department of Materials Science and Engineering, The University of Sheffield, Sheffield S1 3JD, UK
[e] F.A. Finger Institute for Building Materials Science, Bauhaus-University Weimar, Coudraystr. 11, 99421 Weimar, Germany

A R T I C L E I N F O

Keywords:
CSA cement
minor elements
scale-up
ferrite
clinkering
waste valorisation

A B S T R A C T

The production of ferrite-rich calcium sulfoaluminate belite (CSABF) cement clinker, also containing MgO, from ladle slag, Fe-slag, and phosphogypsum was translated from a lab-scale to a pilot demonstration in a 7-metre kiln at 1260 °C. An account of the pilot trials/manufacturing is presented, and the process was robust. Laboratory tests prior to scale-up showed that gehlenite formation can be inhibited in the CSABF clinker by adding excess CaO in the raw meal; however, this reduces the amount of iron (Fe) that can be incorporated into ye'elimite and leads to higher ferrite (C_6AF_2) content. Detailed microstructural analyses were performed on the clinker to reveal the clinker composition as well as the partition of the minor elements. Different ferrite phases with varying amounts of titanium and iron are distinguished. Eighty-five percent of the clinker raw meal was comprised of side-stream materials and the clinker produced in the kiln had chemical raw-material CO_2 emissions 90% lower than that of Portland cement made from virgin raw materials. These results can have a significant impact in regions with a prospering metallurgical industry, enabling industrial decarbonisation and resource efficiency.

1. Introduction

The worldwide manufacturing of 4Gt of cement per year [1] emits more than 3Gt of CO_2. More than half of the emissions arise from the breakdown of calcium carbonate ($CaCO_3 \rightarrow CaO + CO_2$) into raw meal, and the remainder is mainly from the combustion of fuels to reach the high temperature required in conventional cement rotary kilns (~1450 °C) [2].

Natural limestone (mainly $CaCO_3$) is the only realistic calcareous source for large-scale cement manufacturing. Therefore, a reasonable option to lower the CO_2 emissions of cement production is to change the chemical composition of the cement [2] to require less calcium. Alternative binders can lead to significant emission reductions. Cements containing ye'elimite, commonly known as calcium sulfoaluminate (CSA) based cements, are one of the important alternative types with a reduced carbon footprint as the production process requires less calcium carbonate to be calcined and has a lower production temperature. CSA clinker can also be produced in existing cement plant configurations without major modifications or capital expenditures. The modifications required may include better control of the process temperature and residence time, and more accurate clinker phase determination [3]. Due to the volatile nature of CSA constituents at clinkering temperatures, monitoring/controlling the atmospheric conditions is also a crucial aspect of CSA clinker manufacturing [4–7].

CSA based cements are currently in commercial production throughout the world, though most notably in China [8] and North America [9,10], where they have been commercially used for decades in both structural and non-structural applications; however, the use of CSA cements has been limited in Europe due to the lack of standardisation for construction applications and inexpensive raw materials containing

---

Cement oxide notation: C, CaO; S, SiO_2; A, Al_2O_3; F, Fe_2O_3; $, SO_3; M, MgO; T, TiO_2.

[*] Corresponding author.

E-mail address: timo.fabritius@oulu.fi (T. Fabritius).

https://doi.org/10.1016/j.cemconres.2022.106715
Received 8 March 2021; Received in revised form 15 November 2021; Accepted 10 January 2022

alumina. In North America, CSA-based cements have been utilized around 2 million metric tons in the last 30 years [9]. CSA cement is not covered by the harmonized European Standard EN 197-1 but recently has obtained technical approvals for example in Germany [11].

The properties of CSA cements are often superior to those of standard PC, including rapid set and high early strength [8,12]. Despite their higher costs [13], CSA-based cements have been used when extended work-time or closure is not possible, such as the restoration of highway or airfield pavement [9]. CSA-based cements are also used in special applications, such as cements for arctic conditions [8,14], self-levelling cements, expansive cements and cements for waste encapsulation/stabilization [15–17].

One of the main disadvantages of CSA cement production is the price and limited availability of alumina; however, this can be overcome by using aluminium containing waste materials, thus also increasing industrial sustainability through the circularity of resources. The metallurgical industry generates large amounts of inorganic residues that contain the necessary ingredients to produce CSA cement clinker: Al_2O_3, CaO and SiO_2 [18]. The origin of these elements is from slag forming agents (i.e. bauxite, limestone, dolomite, and sand) that are added to a certain process. Utilization of industrial residues in cement manufacture can reduce the price of CSA cements while improving resource efficiency. The usability of metallurgical industry side streams as raw materials for CSA cement production has been tested on the laboratory scale in previous studies [19–21] and various Al_2O_3 bearing alternative by-product-based materials for ye'elimite-rich cement production has been studied in [21–23]. The utilization of iron-rich raw materials leads to formation of ferrite type of solid solution [24,25], that has been studied in PC [2,26], CAC, alite-CSA [27] and CSA cement systems [19,28,29].

In the present study, metallurgical slags from steel and zinc production were used as alternative raw materials in a semi-industrial scale trial to produce a clinker containing Ye'elimite > belite > ferrite. Phosphogypsum, a residue from fertilizer production, was also used as the $CaSO_4$ source; 85% of the raw-meal was consisting of residue. Clay and limestone were used as correctional material to balance the chemical composition in order to achieve target clinker. The utilized residues are high in de-carbonised CaO, thus further reducing the embodied carbon in the raw mix. Synthesized CSABF clinkers were first prepared at laboratory scale from reagent grade chemicals, and then semi-industrial scale (two hundred kilograms) was tested in a 7 m rotary kiln (internal diameter = 0.3 m). Detailed microstructural characterisation is performed on the raw materials and products and the manufacturing process of the clinker in the rotary kiln is explained in sufficient detail to enable the replication and translation to industry.

2. Materials

Laboratory scale testing was conducted on clinkers prepared from reagent-grade chemicals. The tests were carried out to understand how different CaO, Al_2O_3, and SiO_2 contents change the mineralogy of the clinker and to optimise the clinker raw mix for a pilot kiln. The reagent-grade chemicals were aluminium oxide (Al_2O_3; metal basis fine powder; 99%; CAS: 1344-28-1), calcium oxide (CaO; Reagent grade powder; 98%; CAS:1305-78-8), calcium sulphate ($CaSO_4$; anhydrous powder; 99%; CAS:7778-18-1), iron (III) oxide (Fe_2O_3; metals basis powder; 98%; CAS: 1309-37-1) and silicon dioxide (SiO_2; mesh-fused amorphous powder; 99%; CAS: 7631-86-9).

The raw materials for the semi-industrial pilot and reference laboratory clinker were Fe-slag from non-ferrous metal production after pyrometallurgical treatment, ladle slag from steel production, phosphogypsum from fertilizer production and natural raw materials, namely limestone and clay. The chemical composition of raw materials is presented in Table 1. XRD-analysis of ladle slag and Fe-slag can be found from Appendix 1.

Fe-slag is thermally treated jarosite residue from zinc production. The production of 1 t of metal zinc generates around 0.5–0.9 t of jarosite ($ZFe_3(SO_4)_2(OH)_6$, where Z represents either Ag^+, H_3O^+, K^+, Li^+, Na^+, NH_4^+ or ½ Pb^{2+}) [30]. The purpose of pyrometallurgical treatment to jarosite slag is to recover valuable components, and it is water-granulated after firing to obtain an inert amorphous structure and to prevent leaching for safe storage or usage. The product of pyrometallurgically treated jarosite slag is a fayalite-like slag that is called Fe-slag in this study. Fe-slag consists of an amorphous silicate matrix and crystal phases, such as spinel, periclase and magnetite [31]. The ladle slag originates from the secondary metallurgical ladle treatment process of SSAB (Raahe, Finland). In ladle treatments, steel is refined before continuous casting. It is estimated that 1 t of produced crude steel generates 12-15 kg of ladle slag [32]. The major crystal phases of dry ladle slag are gamma belite (γ-C_2S), alite (C_3S), tricalciumaluminate (C_3A), mayenite ($C_{12}A_7$) and periclase (MgO) [33]. Recent studies suggest that around 50 wt% ladle slag consists of the pleochroite/Q-phase ($Ca_{20}Al_{26}Mg_3Si_3O_{68}$) [34]. The mineralogy and alumina content of ladle slag varies among steel plants, and a good review of variations is given in [35]. Phosphogypsum was from Yara (Siilinjärvi, Finland). Approximately 4–6 t of phosphogypsum is produced as a side product when 1 t of phosphoric acid is produced from phosphate rock using sulfuric acid [36]. To balance the composition, when necessary, we used Parfill 500 limestone from Nordkalk (Parainen, Finland) and a high alumina-containing clay originating from China.

Table 1
Chemical composition of raw materials obtained through the XRF (X-ray fluorescence) analysis and LOI (loss on ignition).

Raw material	Fe-slag	Ladle slag	Limestone	Phosphogypsum	Clay
Oxide	wt%	wt%	wt%	wt%	wt%
Al_2O_3	6.8	22.9	0.8	0.1	38.7
CaO	12.2	37.6	50.5	29.1	0.6
Fe_2O_3	49.3	1.6	0.5	0.1	6.1
MgO	1.5	6.1	3.1	0.1	0.4
MnO	0.6	0.7	0.0	0.0	0.0
Na_2O	4.8	0.1	0.1	0.0	0.1
P_2O_5	<0.5	0.0	0.0	0.5	0.1
SiO_2	20.6	8.5	3.6	0.3	38.8
SO_3	0.7	0.5	0.0	39.8	0.0
SrO	<0.3	0.0	0.0	0.5	0.0
TiO_2	0.2	0.9	0.0	0.0	0.6
Others[a]	1.6	0.3	0.2	0.6	0.0
Sum	100.0	79.2	58.8	71.1	85.4
LOI (525 °C, 1 h)	−2.80				
LOI (950 °C, 1 h)	−4.90				
LOI (1000 °C, 1 h)		19.17	41.46	29.31	12.76

[a] Ba, Cu, Cl, Ni and V.

The particle size distribution (PSD) of phosphogypsum, ladle slag, limestone and Fe-slag are presented in Fig. 1. The median particle sizes d_{50} for Fe-slag, ladle slag, phosphogypsum and limestone were 55 μm, 334 μm, 99 μm and 232 μm, respectively. The procedure for PSD is explained in Section 3.1.3.

3. Methods

3.1. Material characterisation

The analyses conducted in this study are shown in Table 2. The study was done in three stages. First the limitations of chemical composition of clinker mixes were tested in laboratory scale (Section 3.2) and then the sufficient clinker mix was selected for pilot (Section 3.3). Finally, the reference sample was prepared with optimal grinding and firing conditions from the same raw mix as in pilot in laboratory scale to compare the quality of the pilot clinker (Section 3.4).

3.1.1. X-ray diffraction

The phase composition of laboratory scale clinkers and

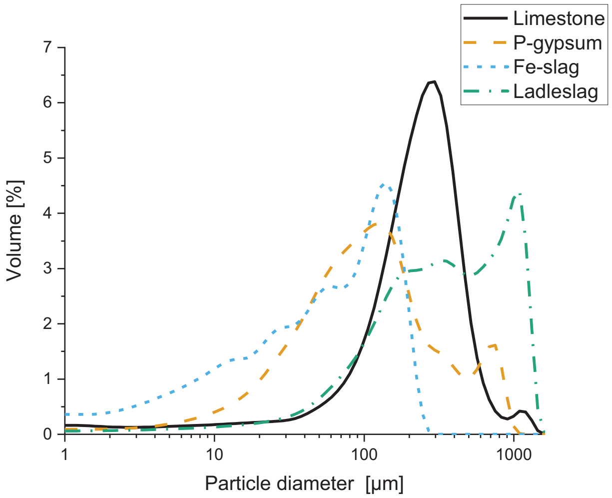

Fig. 1. Particle size distributions of raw materials.

Table 2
Analyses conducted in this study.

Analysis	Raw materials	Pre-tests	Granules	Pilot clinker	Lab clinker
XRD	LS + FE-slag[a]	X		X	X
PSD	X			X	
XRF	X		X	X	
TGA	X				
DTA-TG-MS			X		
SEM + EDX				X	X
Density				X	

[a] Appendix 1.

diffractograms for clinkers during different stages of the clinker burning process were determined using a Rigaku SmartLab 9 kW diffractometer in the Bragg-Brentano geometry. Samples for the XRD analysis were ground to fine powder (<5 µm) by hand using agate mortar for 15 min. The diffractometer was operated with a tube voltage of 45 kV and a tube current of 200 mA. The radiation source used was the Cu Kα X-ray source (Kα1 = 1.54059, Kα2 = 1.54441), and the detector was a D/teX Ultra 250 detector. The patterns were recorded in a range of 2-theta 5–130° with a step size of 0.02° and a scanning speed of 4.063 deg./min, totalling 6251 counts in the XRD-pattern. The phases from the XRD patterns were identified by a Whole Powder Pattern Fit (WPPF) analysis using Rigaku PDXL 2 software with the PDF-4+ 2020 RDB database.

The phase composition and amorphous content of the final clinker and reference clinker was analysed using Siemens D5000 with Cu anode, 200 mm radius, automatic slits, soller slit 2.5° and no filters but an EDS (energy dispersive spectrometry) (detector SolX, Bruker). The diffractometer was operated with 40 kV and 40 mA. The patterns were recorded in the range of 2-theta 5–70° with a step size of 0.02°, totalling 3250 counts in the XRD-pattern. The first sample was run without internal standard and then the amorphous content was refined from second sample using the internal standard method with 20 wt% rutile (TiO_2). The 80-20 mix of the sample and rutile was mixed with the McCrone micronizing mill.

3.1.2. *Particle size distribution*

The particle size distribution (PSD) of raw materials and the ground clinker was measured with a laser diffraction technique using the dry powder system module of Beckman Coulter LS 13 320 with the Fraunhofer model [37]. Because Fe-slag is granulated, it must be further ground. The total 90 kg of Fe-slag was ground in 30 kg batches using a stainless-steel jar mill (TPR-D, Germantec) with the jar diameter of d = 0.6 m and h = 0.6 m. The grinding media consisted of stainless-steel balls of d = 10 mm (20 kg), d = 25 mm (10 kg) and 50 mm (10 kg). The grinding time was 4 h until all the ground material passed a 200 µm sieve. It must be noted that the ladle slag contained some larger rock-like particles of disintegrated ladle slag and some pieces of metal, but for industrially practical reasons, it was not pre-treated. Phosphogypsum contained some gypsum lumps; however, it was found that these lumps disintegrated easily, and it could be assumed that they will break during granulation. Prior to the PSD measurement, phosphogypsum and ladle slag were sieved with a 2 mm sieve and 95.5% and 86% passed, respectively.

3.1.3. *X-ray fluorescence and loss on ignition (LOI)*

The X-ray fluorescence (XRF) analysis from melt-fused beads was used to determine the chemical composition of the raw materials, granules, kiln inlet material and clinker. The Fe-slag and clinker were analysed using the Omnian Pananalytics Axiosmax 4 kV spectrometer. The Fe-slag sample was collected from pre-ground (d_{50} 55 µm) bulk and was then ground with a planetary mill with 300 rpm for 1 min. Loss on ignition (LOI) was measured from ground Fe-slag using the thermo gravimetric analysis TGA (Prepash, Precisa). The heating cycle in TGA was a 30 min ramp to a 105 °C/4 h hold, 2 h 30 min ramp to a 525 °C/3 h hold and 1 h ramp to a 950 °C/3 h hold. The melt fused bead from Fe-slag was prepared by mixing 1.5 g of Fe-slag in a platinum crucible with 7.5 g of X-ray flux Type 66:34 (66% LiB_4O_7 and 34% $LiBO_2$). The fluxing of the bead was done using the Pananalytics Eagon 2 fluxer with a melting temperature of 1200 °C. The rest of the raw materials were analysed using a Bruker S8 Tiger. Alternatively, for the XRF analysis, the loss on ignition (LOI) was determined by difference weighing: 1.5 g of sample material was placed in a preheated corundum crucible and heated to 1000 °C for 1 h. For the measurements, the samples were prepared as fused beads using Spectromelt A12 (66% $Li_2B_4O_7$/34% $LiBO_2$) as flux. 1 g of the preheated sample material was mixed with 8 g of flux and molten in an automatic electric furnace (xrfuse2, XRF scientific) using Pt/Rh crucibles. The measurements were done with a wavelength dispersive X-ray spectrometer (S8 Tiger, Bruker) under vacuum conditions.

3.1.4. *DTA-TG-MS*

A simultaneous differential thermal analysis (DTA), thermogravimetric analysis (TG) and mass spectrometry (MS) were conducted to determine the gasses emitted at certain temperatures during clinkering from the granules. The granule sample was ground with agate mortar, and 25.22 mg of the sample was placed on an alumina crucible. The heating ramp for DTA-TG-MS (STA449 F3 Jupiter, Netzsch and QMS403D Aëolos Quadro, Netzsch) was set to 10 °C/min from room temperature to 1300 °C. The test was run in an argon atmosphere with a gas flow of 60 ml/min. For mass spectrometry, selected ions to be analysed were $m/z = 17$ (OH), 18 (H_2O), 28 (CO), 44 (CO_2), 48 (SO), 64 (SO_2) and 80 (SO_3). In the mass spectrometer analysis, OH/H_2O, CO_2 and SO_2 were detected.

3.1.5. *Scanning electron microscopy (SEM)*

3.1.5.1. Sample preparation. Ground clinker (d_{50} = 6.78 µm) was collected from the batch, pressed to a tablet and embedded into epoxy resin. Sample polishing was carried out using an automatic polishing device (TF250, JeanWirtz, Germany) and diamond oil pastes (MetaDi II, Buehler, US). Successive polishing with oil-based diamond pastes of sizes of 15, 9, 3, 1 and 0.25 µm was applied. To achieve electric conductivity, the polished section was coated with approximately 8–10 nm carbon.

3.1.5.2. SEM imaging and EDX spectroscopy. Back-scattered electron (BSE) imaging and EDX spectroscopy were used for microstructural characterisation (i.e. imaging, elemental mapping and analysis of chemical composition of the major phases) of the produced clinker. BSE imaging and an EDX-analysis were carried out at a 7 kV acceleration voltage and a 0.8 respectively 1.6 nA electron current using a high-resolution field emission SEM (Helios G4UX, ThermoScientific, USA), respectively. For the acquisition of EDX data, two silicon drift detectors were used in parallel (UltimExtreme and X-Max80, Oxford Instruments, UK). This allowed for collecting elemental distribution maps at a high resolution (approx. 0.1 μm pixel resolution). Based on the high-resolution mapping data, areas for EDX spot analyses were selected. The EDX data acquisition and analysis were performed using commercial software (Aztec 4.3, Oxford Instruments, UK). The quantification of the composition of clinker phases was achieved by the calibration of the SEM-EDX setup against a pure cobalt standard. Iron content was determined using Fe-L line. All other elements were quantified using the K-alpha lines of the respective elements.

3.1.6. *Density of the clinker*

A Micromeritics AccuPyc II 1340 Gas Pycnometer was used to measure the density from two samples of semi-industrial pilot clinker with masses of 6.65 g and 6.55 g at 22.9–23.1 °C, respectively. Helium was used as a probe gas, the run pressure was set to 19.5psig and the pressure equilibration was 0.005psig/min. Both samples were run for 10 cycles to improve accuracy. The standard deviations for samples 1 and 2 were 0.0012 and 0.0015, respectively, and the average density of the pilot clinker was calculated from these total 20 runs.

3.2. *Laboratory pre-experiments*

Ten grams of six different clinkers were produced and are referred to here as C1-C6. Prior to weighting, all reagent grade chemicals were dried at 500 °C in a muffle furnace for 12 h and then mixed using mortar and pestle. Then, C1-C6 clinkers were simultaneously fired in alumina crucibles in the same muffle furnace. The crucibles were placed in the muffle furnace at 800 °C, heated with a ramp rate of 7.6 °C/min (~1 h) to 1260 °C and held for 1 h. Next, the crucibles were removed from the furnace, and the pyro-processed materials were poured from the crucibles on a copper table to cool in ambient air.

The chemical compositions to acquire the desired phases for target laboratory scale clinkers were calculated using the equations presented in Table 3. Gypsum $CaSO_4$ (41 wt% CaO; 59 wt% SO_3) was used as a SO_3 source. The amount of $CaSO_4$ was calculated according to $SO_3/0.59$, and the required CaO was adjusted with CaO - (C$*0.41). The target phase composition and chemical composition for laboratory scale clinkers are presented in Table 4. The target composition for the C1 clinker was 45 wt% ye'elimite (C_4A_3\$), 38 wt% belite (C_2S), 15 wt% ferrite (C_4AF) and 2 wt% anhydrite C$. The target was modified in C2-C6 to understand how different CaO, Al_2O_3 and SiO_2 contents change the mineralogy of the clinker. Free C$ was targeted in all the clinkers to compensate for possible SO_3 loss during firing and to maximise ye'elimite formation over mayenite.

Table 3

Molar masses and equations used to calculate the target phase composition.

Oxide	Molar mass oxide [g/mol]	Phase	Molar mass phase [g/mol]
Al_2O_3	101.96	C_4AF	485.96
CaO	56.08	C_2S	172.24
Fe_2O_3	159.69	C_4A_3\$	610.26
SiO_2	60.08	C$	136.34
SO_3	80.06	–	–

Equations

Al_2O_3 = [C_4A_3\$ (wt%) / (C_4A_3\$ (g/mol) / 3 * Al_2O_3 (g/mol)] + [C_4AF (wt%) / (C_4AF (g/mol) / Al_2O_3 (g/mol)]

CaO = [C_4A_3\$ (wt%) / (C_4A_3\$ (g/mol) / 4 * CaO (g/mol))] + [C_4AF (wt%) / (C_4AF (g/mol) / 4 * CaO(g/mol))] + [C_2S (g/mol) / (2 * CaO (g/mol))] − C$ (wt%) * 0.41

Fe_2O_3 = [C_4AF (wt%) / (C_4AF (g/mol) / Fe_2O_3 (g/mol))]

SiO_2 = [C_2S (wt%) / (C_2S (g/mol) / SiO_2 (g/mol))]

SO_3 = [C_4A_3\$ (wt%) / (C_4A_3\$ (g/mol) / SO_3 (g/mol))] + [C$ (wt%) / (C$ (g/mol) / SO_3 (g/mol))]

3.3. *Pilot experiments*

3.3.1. *Granulation*

The raw materials used in the trials were weighted, mixed, and granulated to achieve a homogenous mix and to prevent material losses that might occur due to high gas velocity from the burner during firing. Prior to the actual granulation, the required water content needed was first tested on the laboratory scale using a mixer (R02, Eirich). For the pre-test, granules between 1 mm and 5 mm were achieved with a 5 wt% water addition. The actual granulation was done using a mixer equipped with star pin rotor (R11, Eirich). An image of the wet granules is presented in Fig. 2. The granulation was done in 150 kg batches, and the following steps were used: 1) weighting the materials and loading the machine; 2) dry mixing 1 min with a rotor speed of 700 rpm; 3) addition of tap water (5 wt%) and continue with 700 rpm for 5 min; 4) granulation with 600 rpm for 5 min; and 5) discharging of wet granules through the bottom opening on a dispenser disk to 200 l steel drums.

3.3.2. *Pilot kiln and operating conditions*

The 24-hour kiln trial was conducted at the facility of IBUtec AG in Weimar. The same kiln has successfully been used for the pilot testing of ternesite-based CSA [38] and belite calcium sulfoaluminate clinkers from previous studies [39]. The granulated raw material mixes were fired in a 0.3 m ID × 7 m rotary kiln at ~1260 °C for the present investigation. During the trial, SO_2, CO and CO_2 gas flow from the kiln as well as the consumption of O_2 and natural gas were measured by a gas analysis. CO, CO_2 and SO_2 measurements were based on NIR (Near-infrared) analyses, and the O_2 – measurement was based on paramagnetic sensors. The temperature of the kiln was monitored with six thermocouples, and the actual temperature at the burning zone was measured each hour using a handheld Keller CellaPort PT 140 thermometer. The quality of the clinker was examined through the XRD analysis.

The pilot setup consisted of mixer/granulator, belt feeder, kiln tube, a cyclonic kiln dust separator, a dust baghouse filter, an exhaust extractor fan, a burner and oxygen feeding system. The setup and process parameters of the kiln are presented in Table 5, and the simplified flow sheet of the experimental setup is presented in Fig. 3. First, the weighted raw material mix was granulated in four batches. The raw mix presented in Table 6 was calculated using the target composition C6 (see Table 4) and the chemical and LOI analyses from Table 1. For C6, excess CaO was added to prevent gehlenite formation and excess $CaSO_4$ to ensure the formation of ye'elimite over mayenite, as previously discussed. Granulation was performed for the raw materials to achieve a homogenous mix and to prevent material losses that might be caused by the gas flow in the kiln during firing. The granule size was between 1 mm and 5 mm.

The wet granules were fed via a belt feeder into a kiln hopper. The total residence time and time in the burning zone of the material in the kiln was estimated to be 3 h total and 0.7 h in the burning zone, which is the last 1.5 m of the kiln before the burner head. Feeding to the belt was operated manually. At the beginning of the trial, the feeding speed was 25 kg/h, but it was reduced to 20 kg/h because 4 kg/h (20%) of the material was lost as kiln inlet material. The material loss was mainly caused by the air flow from the burner.

With 20 kg/h feeding, the product rate was ~10 kg/h. Half of the mass of the raw material feed was lost due to the loss of H_2O, CO_2 and SO_2 from the mix as well as because the airflow in the kiln carried some of the material back to the kiln inlet. The kiln was directly heated with a burner using natural gas. The average natural gas consumption during the trials was $20.1 Nm^3/h$ (N stands for normal P and T). To decrease the

Table 4
Target compositions and chemical composition of laboratory scale clinkers. The target composition for C1 clinker was 45 wt% ye'elimite $C_4A_3\$$, 38 wt% belite C_2S, 15 wt% ferrite C_4AF and 2 wt% anhydrite C$. The normalised chemical composition to 100 wt% is presented in brackets.

	Clinker	C1	C2	C3	C4	C5	C6
Δ target composition ±g	CaO	0	+5 g	−5 g	+5 g	+5 g	+0.7 g
	SiO_2	0	0	0	0	+1.5 g	−0.7 g
	Al_2O_3	0	0	0	+2.5 g	0	0
Target chemical composition wt%	Al_2O_3	25.7	25.7 (24.5)	25.7 (27.1)	28.2 (26.2)	25.7 (24.1)	25.7
	CaO	49	54 (51.5)	44 (46.3)	54 (50.3)	54 (50.7)	49.7
	Fe_2O_3	4.9	4.9 (4.7)	4.9 (5.2)	4.9 (4.6)	4.9 (4.6)	4.9
	SiO_2	13.3	13.3 (12.6)	13.3 (14)	13.3 (12.3)	14.8 (13.9)	12.6
	SO_3	7.1	7.1 (6.7)	7.1 (7.5)	7.1 (6.6)	7.1 (6.6)	7.1
	Total	100	105 (100)	95 (100)	107.5 (100)	106.5 (100)	100

Fig. 2. Wet granules before firing produced using the R11 Eirich mixer.

Table 5
Process parameters of the kiln trial.

Operation	Used in trial
Kiln length	7.4 m (7.0 m heated)
Kiln inner diameter	0.3 m
Refractory thickness	5 cm
Kiln inclination	1.0°
Kiln rotation speed	2 rpm
Heating method	Direct heating
Operating configuration	Counter current flow
Residence time	3 h
Raw meal feed (wet)	20–25 kg/h
Raw meal feed (dry)	15–19 kg/h
Natural gas flow rate	20.1 ± 0.6 m^3/h
Oxygen flow rate (burner)	5 m^3/h
Oxygen volume kiln inlet	4.9 ± 0.7 Vol.-%
Clinkering zone temperature	1260 ± 6.5 °C
Exhaust cleaning	Dust filter, cyclone

gas flow and to compensate for heat loss in the kiln, pure oxygen was added at a rate of $5 m^3/h$ into the primary air of the burner. To obtain oxidizing conditions, the oxygen content in the kiln inlet head was adjusted to about 5 Vol.-% with secondary air. The actual value for oxygen during the trial was measured to be 4.9 ± 0.7 Vol.-%.

Exhaust SO_2 gas was measured by near infrared analyses (NIR) every 2 h from the kiln inlet and after the baghouse filter, as shown in Table 7. The average content of exhaust SO_2 during the trial was around 48 ppm, and the highest values were recorded in the final hours of the trial. The SO_3 loss was not significant when clinkering at 1260 °C. Exhaust CO and CO_2 were also measured with NIR from the kiln inlet. The amount of CO_2 exhaust gas flow was 10.5 ± 0.5 Vol.-%, and the amount of CO was constantly below 0.1 Vol.-%. The total gas flow to the kiln was $238 m^3/h$, from which 164 m^3/h was primary air to the burner and 55 m^3/h was secondary air to adjust the O_2 level in the kiln.

The temperature profile of the kiln is presented in Table 8. The temperature during the trial was controlled and monitored with thermocouples presented in Fig. 3, and the temperature at the burning zone was measured hourly with a digital pyrometer (Keller CellaPort PT 140).

The clinker was cooled in the last 0.4 m after the burner before being discharged from the kiln. It was estimated that the clinker will cool to ~1000 °C over a 10 min timescale before being discharged from the end of the kiln onto a metal tray, where it was left to cool in air; due to low throughput (~10 kg/h), cooling was assumed to be rapid.

3.3.3. *Grinding and mixing of the clinker*

The clinker produced in the first 45 min was disposed of, and then 14 buckets totalling around 240 kg of the clinker was collected and packed in airtight plastic buckets. The clinkers from each of the 14 buckets were separately ground using a ball mill with the same technique as for Fe-slag with the difference that the clinker was ground for 2-3 h until >85% of the material passed the 45 μm sieve. Ground clinkers from the buckets were mixed using a shovel brush and a tarpaulin. First, all the clinkers were poured from the buckets side by side on a tarpaulin and then mixed in the opposite direction, and then the premixed clinker was piled up and mixed using a quartering method. For the quartering method, the piled clinker was first mixed several times, and then the pile was flattened and divided into quarters. Two opposite quarters were removed, and the previous steps were repeated for the remaining two quarters until there was around 20 kg of clinker left to fit in the bucket. Samples for PSD, density, XRD and XRF analyses were collected to represent the whole 240 kg. The quartering was repeated until all clinker was mixed and placed into buckets again.

3.4. *Comparison of pilot clinker to clinker made from ground granules*

The particle size of raw materials was relatively high for clinkering. Therefore, a reference sample from the granules presented in Table 6 was dried, ground to fine powder ($d_{50} = 8$ μm) using disc mill (Retsch, RS 200) and fired in laboratory scale muffle furnace. The clinker was then compared to the results of XRD and SEM-analysis of pilot clinker.

4. Results

4.1. *Findings from lab-scale clinker production using reagent grade materials*

Ten grams of each laboratory scale clinker were produced with labels C1-C6 (see Table 4). The target composition for the C1 clinker was 45 wt % ye'elimite ($C_4A_3\$$), 38 wt% belite (C_2S), 15 wt% ferrite (C_4AF) and 2 wt% anhydrite C$. The target was modified in C2-C6 to understand how different CaO, Al_2O_3 and SiO_2 contents change the mineralogy of the clinker and to understand the effect of fluctuations in raw material feeds.

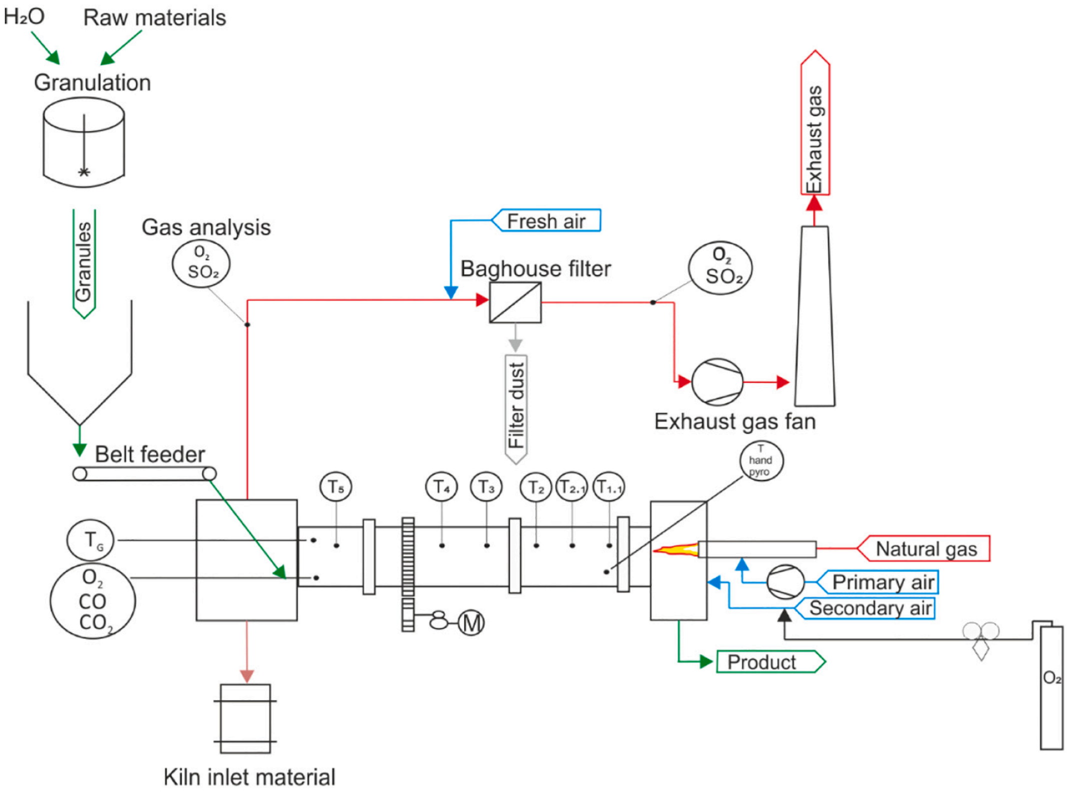

Fig. 3. Simplified flowsheet/description of the rotary kiln configuration used in the pilot plant trials.

Table 6
Granulation recipes of raw materials mixes.

Unit	Ladle slag	Fe-slag	Phosphogypsum	Clay	Limestone	Added water	Weight of mix
kg	106.5	6.0	18.0	6.0	13.5	6.5	150
wt%	68.1	3.8	11.5	3.8	8.6	4.2	100

Table 7
SO_2-gas analysis from the kiln inlet and after a baghouse filter.

Analysis point	SO_2 raw gas [ppm]	SO_2 after baghouse filter [ppm]
Lowest	5	21
Highest	88	77
Average (12 analysis points)	59	48
Stdev.	37	17

Table 8
Kiln temperature measured with thermocouples (see Fig. 3) and a handheld thermometer.

	T5	T4	T3	T2	T1.2	T 1.1	Burning zone
Position	0.2 m	1.7 m	3.3 m	5	6.1 m	6.5 m	7.0 m
Average [°C]	519.4	821.7	948.8	1109.4	1227.2	1231	1260.4
St. dev. [°C]	13.9	10.8	11.7	13.7	15	12.2	6.5

Table 9
XRD results for a sensitivity analysis on raw meal fluctuations conducted for C2-C6.

	Clinker	C1	C2	C3	C4	C5	C6
Δ target composition ±g	CaO	0	+5 g	−5 g	+5 g	+5 g	+0.7 g
	SiO_2	0	0	0	0	+1.5 g	−0.7 g
	Al_2O_3	0	0	0	+2.5 g	0	0
Result XRD [wt %]	$C_4A_3\$$ [39]	40	35.1	49.1	36.6	38.5	38.6
	C_2S [40]	44.8	48.1	42.4	48.8	45.4	42.6
	$C_2(A,F)$ [25]	9.8	14.1	3.6	12.7	13	15
	$C\$$ [41]	1.2	0.8	0	1.2	1.4	1.2
	$C_{12}A_7$ [42]	4.1	1.9	0	0.7	1.7	2.7
	C_2AS [43]	0	0	4.9	0	0	0
	R_{wp} [%]	4.19	4.91	4.08	4.28	4.62	4.55

The results of the sensitivity analysis of lab-scale clinkers C2-C6 carried by the XRD analysis are presented in Table 9.

The sensitivity analysis showed that the amount of CaO is critical to phase composition. In Fig. 4, C1 is the base composition, and the compositions C2-C6 are derived from C1 to study the effect of CaO, SiO_2 and Al_2O_3 on phase formation. It was observed that a 5% decrease of CaO in C3 from the target composition C1 leads to the formation of gehlenite (C_2AS), which is an undesired non-hydraulic phase. A 5% increase of CaO in C2 compared to target composition (C1) increases the

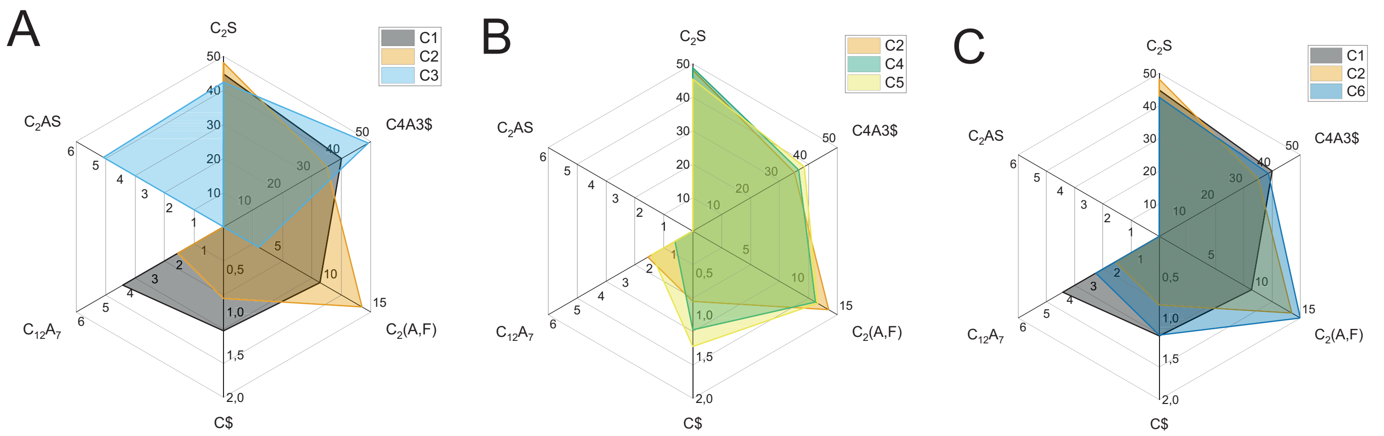

Fig. 4. The phase compositions in (XRD results, wt%) of laboratory scale clinkers.

amount of C_2S and $C_2(A,F)$ formed but also reduces the amount of $C_4A_3\$$ and $C_{12}A_7$ and C$; however, no non-hydraulic clinker phases, i.e. gehlenite (C_2AS) was formed. It was observed that a 5% decrease of CaO in C3 from the target composition C1 leads to the formation of gehlenite. In addition, decreasing the amount of CaO in the raw materials reduces the amount of ferrite and increases the amount of ye'elimite. Ye'elimite formation in C3 is above target, thus suggesting increased Fe incorporation into ye'elimite when CaO is reduced. How an increase in Al_2O_3 (C4) and SiO_2 (C5) coupled with an increase in CaO affects the target composition was also tested. It was found that SiO_2 or Al_2O_3 addition with CaO changed the final mineral composition only slightly. In C6, 2 wt% C_2S was replaced with 2 wt% CaO in the target when compared to C1 to prevent gehlenite formation. Based on these findings, as shown in Fig. 4, CaO must be optimised to prevent gehlenite formation, and excess CaO is consumed by the cementitious clinker phases. The composition C6 was selected for pilot kiln testing.

4.2. *Findings of the pilot kiln trial*

During soak calcination on relatively small amounts of material in a muffle furnace, the temperature and residence time are well-controlled; however, the translation of the results to a scaled-up process using a rotary kiln is complex and must be tested as the material will be mobilised in a flowing and continuously renewed gas atmosphere. To prove the industrial feasibility of CSABF clinker manufacturing from the specified residues, the laboratory tests were scaled up using industrial grade raw materials in a directly heated rotary kiln with a counter current flow.

Virgin raw materials for CSABF cement, such as limestone, clay and bauxite, were 85% replaced by industrial side streams. The industrial raw materials used for this pilot are generally used as landfill and only partly used for low-value reuse-applications. Ladle slag was selected as the alumina source due to its high alumina and CaO content and its availability from the local steel plant. Other possible alumina sources for CSA cements are clay (kaolin), bauxite or other high-alumina industrial residues. The Fe-slag used could also be replaced by other iron silicate slag, such as fayalite slag from nickel production [19]. The use of slags containing already decarbonized CaO instead of $CaCO_3$ led to remarkably lower CO_2 emissions from clinker manufacturing. CO_2 emissions from limestone in a raw mix were calculated to be 51 kg/t, which is 90% lower than that of Portland Cement made from virgin raw materials.

4.2.1. *Raw material treatments and analyses*

Moisture content and LOI of the raw materials are presented in Table 10. Fe-slag, limestone and clay were dry materials, but ladle slag and phosphogypsum were wet and contained moisture. The majority of the LOI from ladle slag is obtained under 500 °C and is caused by evaporating water and the decomposition of hydrated phases with crystal water (AFm, CSH etc.) and OH-groups (hydrogarnet, $Ca(OH)_2$, Al $(OH)_2$, etc.). A mass loss of phosphogypsum is also associated with the evaporation of water when gypsum transforms into anhydrite. From limestone, CO_2 is lost between 500 and 1000 °C. Iron containing Fe-slag has a negative LOI due to iron-containing phases oxidized at higher temperatures. The chemical composition of raw materials is presented in Table 1.

Table 10
Moisture content and LOI of the raw materials.

	Moisture (125 °C, 1 h) [wt%]	LOI (500 °C, 1 h) [wt%]	LOI (1000 °C, 1 h) [wt%]
Fe-slag	0.03	−2.27	−4.57[a]
Limestone	0.03	0.48	41.49
Ladle slag	14.11	24.93	25.42
Phosphogypsum	25.64	28.86	29.31
Clay	1.45	6.85	13.75

[a] Oxidation of FeO leads to negative LOI.

The granulation process is explained in Section 3.3.1. Wet granules were analysed by XRF to determine the chemical composition, and the DTA-TG-MS was conducted to analyse/simulate the behaviour of granules during clinkering. Before the XRF analysis, the LOI for granules and kiln inlet materials was measured to be 17.5 t.-% and 9.5 wt% at 950 °C, respectively. As shown in Table 11, the XRF analysis of granules and kiln inlet materials indicated that the chemical composition of kiln inlet materials is almost the same as that of granules, with a slight difference between CaO and Fe_2O_3 quantities. The DTA-TG and mass spectrometer curves are presented in Fig. 5.

The strong endothermic effect below 200 °C is mostly associated with moisture evaporation and the decomposition of crystal water from gypsum first to hemihydrate and then to anhydrite, which could be detected as mass spectrometry peaks $m/z = 17(OH)$ [44]. The weight losses between 200 °C and 400 °C can be associated with the decomposition of hydrates. The decomposition $Al(OH)_3$ was observed as a small lump at 300 °C. Total water loss from raw meals leads to a 20 wt% mass loss. Limestone ($CaCO_3$) decomposes around 700 °C and is shown as $m/z = 44(CO_2)$. The clinker phases start to form above 800 °C, which is shown as multiple small peaks in the DTA curve. The decomposition of phosphogypsum (anhydrite) can be observed as the highest peak of $m/z = 64(SO_2)$ at 1215 °C [44]. There is an endothermic DTA peak at 1200 °C, which may indicate the start of partial melting [45]. The second SO_2 peak at 1250 °C indicates the decomposition of SO_3 from ye'elimite to SO_2 and O_2 [46]. The TG curve shows that weight loss due to CO_2 evaporation is around 5 wt% between 600 and 800 °C, and at the clinkering temperature of 1260 °C, the mass loss due to sulfur loss is

Table 11

Oxide composition obtained by the XRF analysis of dried granules and kiln inlet materials (lost materials during firing).

Major oxides [wt%]				
Oxide	Granules	Granules normalised	Kiln inlet material	Kiln inlet material normalised
CaO	43.3	45.2	44.6	46.5
Al_2O_3	21.5	22.4	21.2	22.1
SiO_2	12.3	12.8	12.6	13.1
Fe_2O_3	6.6	6.9	5.4	5.6
SO_3	7.2	7.5	7.1	7.4
MgO	4.9	5.1	5	5.2
Sum	95.8	100	95.9	100

Impurities [wt.%]		
Oxide	Granules	Kiln inlet material
TiO_2	0.8	0.8
MnO	0.7	0.7
Na_2O	0.4	0.4
Cr_2O_3	0.1	0.1
K_2O	0.1	0.2
P_2O_5	0.2	0.2
SrO	<0.1	<0.1
Cl	<0.1	<0.1
BaO	<0.1	<0.1
Nb_2O_5	<0.1	<0.1
NiO	<0.1	<0.1
CuO	<0.1	<0.1
ZrO_2	<0.1	<0.1
ZnO	<0.1	<0.1
Co_3O_4	<0.1	<0.1
Sum	98.4	98.7

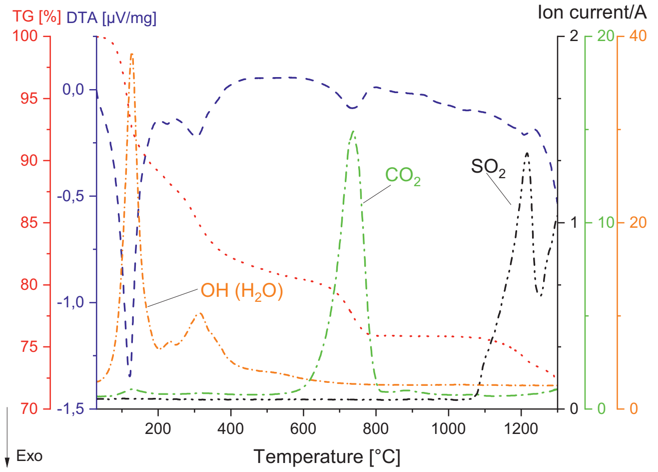

Fig. 5. DTA-TG curves from raw meal granules with a mass spectrometry analysis of H_2O, CO_2 and SO_2 gasses. Argon atmosphere, 10 °C/min 30–1300 °C.

around 2 wt%, which is different in the kiln because there is local build-up of SO_2 pressure [38]. The total mass loss of raw meal according to the TG curve is around 25 wt%.

4.2.2. *Analyses of the pilot clinker*

The results of the XRD analysis of samples obtained during different stages of the clinker burning process are shown in Fig. 6. The XRD analysis suggested that the material was homogenous throughout the trial, with small differences in SiO_2 content. The major phases of the clinker were identified to be ye'elimite $C_4A_3\$$ [39], belite C_2S [40] and ferrite $C_2(A,F)$ [25], and the minor phases were gehlenite C_2AS [43], tricalcium aluminate C_3A [47], anhydrite C\$ [41], mayenite $C_{12}A_7$ [42], periclase MgO [48] and quartz SiO_2 [49].

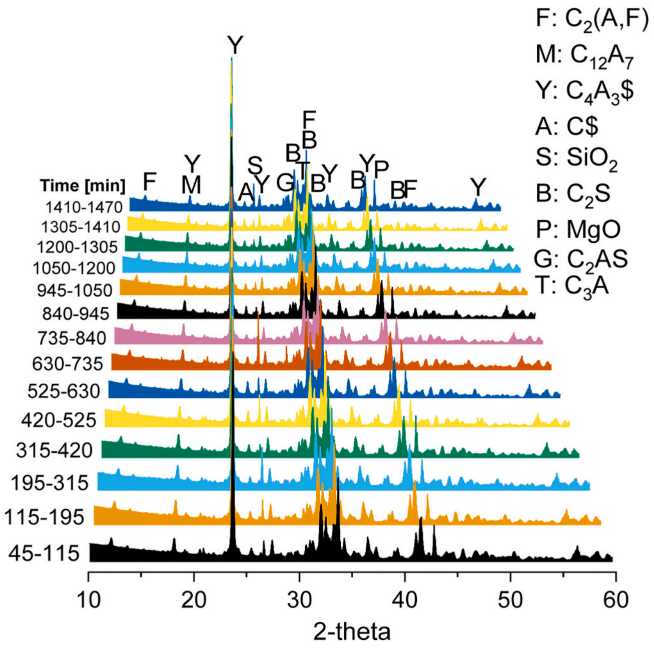

Fig. 6. XRD analyses of clinkers at increasing burning times. F: ferrite $C_2(A,F)$, M: mayenite $C_{12}A_7$, Y: ye'elimite $C_4A_3\$$, A: anhydrite C\$, S: quartz SiO_2, B: belite C_2S, P: periclase MgO, G: gehlenite and T: tricalcium aluminate.

The unground clinker after firing is presented in Fig. 7. The clinker was ground and mixed as mentioned in Section 3.3.3. The particle size distribution of the ground clinker is presented in Table 12. 87.5% of the particles was under 45 µm, and the median particle size value (d_{50}) of the pilot clinker was 6.78 µm. The density of the produced clinker was 3.155 g/cm^3.

The XRD-analysis of ground pilot clinker was compared to reference sample burnt in a small laboratory furnace (Section 3.4) to assure the homogeneity of the pilot kiln process. The XRD-pattern of the homogenized pilot clinker (red line) from the entire trial with comparison to reference clinker prepared from ground granules (black line) with peak identification is presented in Fig. 8. Results show that both clinkers are made up of the same phase assemblage. The peak intensities indicate that in the pilot clinker some more unreacted or intermediate phases are present, i.e. mayenite, gehlenite, anhydrite and quartz. Quantification of results is shown in Appendix 2 and 3. This shows that finer grinding of raw mix and lab furnace conditions improve clinker quality.

XRD-Rietveld analysis was conducted to analyse the phase

Fig. 7. Unground clinker after firing. Black particles are iron-rich nodules.

Table 12
Particle size distributions (PSD) of the ground pilot clinker.

Particle diameter [μm]	% below
20	72.2
32	81.7
45	87.5
63	93.1
90	99.3
100	99.9
125	100
250	100

composition of pilot clinker (Table 13). Oxide composition was recalculated using the Rietveld phase abundances shown in Table 14. The target phase composition was reached in the semi-industrial trial at an adequate level. The most notable differences to the target were a lower $C_4A_3\$$ and C_2S content. The $C_4A_3\$$ content could be underestimated because there is a difference in SO_3 content between the recalculated oxide composition from the Rietveld analysis and the XRF analysis (Table 14). C_2S content is explained by unreacted SiO_2 and the formation of gehlenite and merwinite. It was expected that reaching the target was not realistic because the raw material mix was diluted with impurities, most notably MgO. In Portland cement systems, international standards limit the content of MgO in cement to a maximum of 4–6% [50,51], and although CSA cements cannot be directly compared to PC, the values will still be within the limit, especially after blending with gypsum to form a final cement [50].

The chemical composition of the pilot clinker was analysed by the XRF analysis and is presented in Table 14. According to the XRF, the iron content in the clinker was above the target. The target oxides needed to form hydraulic cement phases consisting of around 90 wt% of the clinker, and the main impurity in the clinker was determined to be MgO. From an environmental perspective, the clinker contained only a minor number of impurities. The difference between the XRF analysis results of the granules and the clinker is compared in Table 15. It was found that iron content increases in clinker and sulfur are lost during firing.

4.2.3. SEM-EDX and composition of CSABF clinker phases

To study the mineralogical and chemical composition of the clinker, the SEM-EDX analysis was conducted. The BSE images obtained on pressed tablets of ground clinker are presented in Fig. 9.

The distribution of clinker phases is heterogenous and formed clusters of phases (that were mostly broken during grinding) in the size of tens of micrometres. The sizes of the individual clinker phases is small (i.e. below 5-10 μm diameter, Fig. 9B). The small size of the phases required high resolution EDX mapping data to determine the composition of individual phases. The clinker microstructure shown in Fig. 9B is characterised by an intensive intergrowth of hypidiomorphic crystals. The microstructure of the pilot clinker is compared to reference clinker from ground granules in Appendix 3 and it shows that the homogeneity of the clinker could be improved by grinding of the raw mix.

Table 13
Phase composition of mixed pilot clinker analysed with Rietveld method. Error of analysis and quality of the analysis R_{wp} were obtained from analysis software.

Phase	Reference	Pilot clinker [wt%]	Target phases [wt%]	Reference clinker [wt%]
$C_4A_3\$$	[39]	31.3	45.0	34.4
C_2S	[52]	28.9	36.0	25.9
$C_2(A,F)$	[25]	8.7	15.0	9.1
$C\$$	[41]	1.7	2.0	1.7
$C_{12}A_7$	[42]	2.0	0.0	0.1
C_2AS	[43]	6.1	0.0	1.9
M	[48]	4.4	0.0	3.4
S	[49]	1.4	0.0	1.4
$C_3T(F,A)$	[53]	0.6	0.0	0.2
C_3A	[47]	5.3	0.0	9.3
K_2SO_4	[54]	2.6		2.6
A	[55]	0.2		0.1
C_2F	[25]	2.7		4.2
CT	[56]	0.2		0.4
Spinel (TF)	[57]	1.6		3.5
C_3MS_2	[58]	2.4		4.6
C		0.0	2.0	0.0
Amorphous		2.7[a]	0.0	n.d.
R_{wp} [%]		10		11

[a] Amorphous content was analysed with separate sample with internal standard.

The EDX phase distribution map is based on elemental mappings, examples of elemental maps is shown in Fig. 10. A prerequisite for the selection of areas for a EDX analysis is a high-resolution EDS mapping (Fig. 10). The shown phase distribution maps possess a pixel resolution of 100 nm.

The phase map (PM) of the clinker (Fig. 10, PM) was deduced using the phase clustering algorithm implemented in the software Aztec 4.3 (Oxford Instruments). The number of detected phases was reduced by merging the segmented phases to one phase. The results of the cluster analysis led to the differentiation of eleven different phases. Ye'elimite, belite, ferrite and periclase were identified to be in good agreement with the BSE image. In addition to the regular ferrite, one other ferrite type is present that can be differentiated by an increased titanium content. Furthermore, tricalcium aluminate (C_3A) and Ca-Al-Si-S phase (CAS (\$)) were found next to or within ye'elimite and belite (Fig. 10 PM). The Ca-Al-Si-S phase is of a very small size, and thus the determination of the chemical composition might be affected by neighbouring phases. Residues of raw materials are present as FeO, K-Al-Si-oxide, C_3A and SiO_2.

The chemical composition of the phases was determined by the SEM-

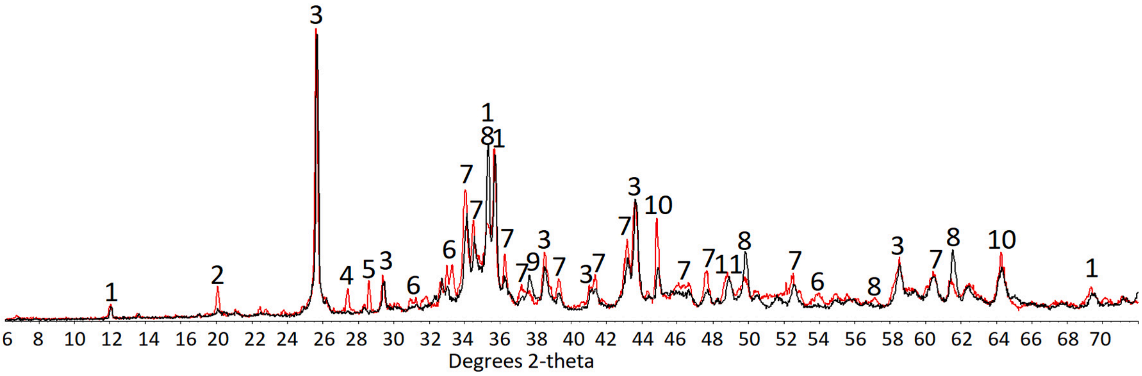

Fig. 8. XRD-pattern of CSABF pilot clinker (red line) with phase identification and reference sample prepared in laboratory furnace from ground granules (black line). 1: $C_2(A,F)$, 2: $C_{12}A_7$, 3: $C_4A_3\$$, 4: $C\$$, 5: SiO_2, 6: C_2AS, 7: C_2S, 8: C_3A, 9: Al_2O_3, 10: MgO, 11: K_2SO_4. The detailed analyses can be found in Appendix 2. (For interpretation of the references to colour in this figure legend, the reader is referred to the web version of this article.)

Table 14
Recalculated oxide composition from Rietveld phase abundances. Oxide compositions were obtained by XRF analysis of mixed pilot clinker. The original elemental wt% obtained from the analysis is converted to oxides.

Major oxides			
Oxide	Rietveld back calculation [wt%]	XRF [wt%]	XRF normalised [wt%]
CaO	42	42.3	44.3
Al_2O_3	24.7	20.9	21.9
SiO_2	13.9	12.5	13.1
Fe_2O_3	5.6	9.7	10.2
SO_3	6.5	5.2	5.5
MgO	4.8	4.8	5
Sum		95.2	100

Impurities [wt%]		
Oxide	Rietveld back calculation [wt%]	XRF [wt%]
TiO_2	1.1	0.8
MnO		0.8
Na_2O		0.3
P_2O_5		0.2
Cr_2O_3		0.1
K_2O	1.4	0.1
SrO		0.1
Cl		0.1
BaO		0.1
Nb_2O_5		<0.1
NiO		<0.1
CuO		<0.1
ZrO_2		<0.1
ZnO		<0.1
Co_3O_4		<0.1
Sum		98.1

EDX spot and area analysis on the same area as the mapping data shown in Fig. 10. The advantage of this approach is that the spots can be placed on areas where only a single phase is present (which is often not possible if the spots are positioned based on BSE information only). For the chemical analysis, 10 spot analyses were performed for each major phase identified with the cluster analysis. The data were collected from the middle of the crystals to minimise overlap with other phases. The results of the SEM-EDX point analyses are presented in Table 16. In addition, the sum spectra for all areas that were segmented as ferrite and Ti-ferrite were quantified (Table 16). The advantage of these sum spectra is an increased number of X-ray counts as compared to single point analyses, therefore quantification of minor elements is possible. Results for ye'elimite, ferrite and Ti-ferrite sum spectra are included to Table 16.

As shown by the results in Table 16, clinker phases contained minor elements in addition to their major elements. The incorporation of minor elements mainly leads to the observed deviation from an ideal phase composition. The acceleration voltage for the analyses was set to 7 kV. Thus, it can be assumed that the determined phase composition is only negligibly affected by neighbouring phases (i.e. excitation volume were X-rays emerge in alite has a diameter of approx. 1 µm at 7 kV). By EDX point analysis, impurities from industrial raw materials, such as Mg, Na, P and Ti, were detected in clinker phases. The standard deviation of the spot analyses can be quite high, especially for minor elements (Table 16). The reason is the lower data quality (peak/background) and the effect of overlap analyses from neighbouring phases for spot analyses. Using the sum spectra for quantification implies that many spot analyses are merged to one spectrum for deconvolution/quantification. This improves the data quality (peak/background) and resembles often better the mean composition of phases. Therefore, results in Table 16 show the ferrite compositions as determined from sum spectra. Generally, phase compositions from sum spectra are similar to spot analyses. For ferrite and Ti-ferrite the sum spectra allow to quantify that the Ti-ferrite phase contains an increased Mn but also increased Ca, Al, Mg and S content.

Table 15
Comparison of the normalised amount of target oxides between the granules and the clinker based on XRF-analysis.

Oxide	Clinker normalised	Granules normalised	Change of oxide [wt%]
CaO	44.3	45.2	−2
Al_2O_3	21.9	22.4	−2
SiO_2	13.1	12.8	2
Fe_2O_3	10.2	6.9	32
SO_3	5.5	7.5	−36
MgO	5.0	5.1	−2
Sum	100	100	

The iron is present in two different solid solutions according to the phase map (Fig. 10) and results in Table 16: Ferrite and titanium rich ferrite both possess a high Fe/Al ratio. Ti-ferrite had Al/Fe ratio close to 1 and some iron was replaced with titanium. Composition of Ti-ferrite is regarded as a solid solution in the brownmillerite-perovskite ($Ca_2(Fe_{1-x},Al_x)_2O_5$ - $CaTiO_2$) series.

The mole content of ferrite and Ti-ferrite was calculated with five oxygens using the sum spectra in Table 17 and Table 17 shows the chemical composition of Ti-ferrite and ferrite presented as Mol, Mol % and apfu (atoms per formula unit), respectively. The formula for Ti-ferrite is close to $C_2(A_{0.59},F_{0.41})$, where iron is substituted with Mg and Ti. Ferrite can be regarded as iron-rich brownmillerite $C_2(A_{0.19},F_{0.81})$.

Similar to the differentiation of ferrites EDX-analysis allows to distinguish belites and reveals that phosphorus and sodium were mainly incorporated into belite. Although the phase map did not distinguish different belites, element distribution map of S shows that belites with high and low sulfur content are present (i.e. belite-1 and belite-2 in Fig. 11 and Table 18). Quantification of spectra in these areas confirms that belite-1 possesses approximately 3.1 wt.% SO_3, whereas the S-poor belite-2 contains 0.2 wt.% SO_3 (close to detection limit of analysis). In addition to increased SO_3 content also Al_2O_3 is increased in belite-1 (Table 18). Calculation of CaO/SiO_2 of the two belites shows that the SO_3 and Al_2O_3 rich belite has a ratio of 2.1 and belite-2 a ratio of 1.8.

According to the P-element distribution map (Fig. 11) single belites contain an increased P content. Results of EDX analysis on one of these particles is shown in Fig. 11 and Table 18 This belite also has an increased Mg content and low SO_3, Al_2O_3 content (similar to belite-2). The P_2O_5 content is approximately 2.8 wt.%.

5. Discussion

5.1. Pre-tests

The raw meal for the pilot clinker was designed using XRF data of the raw materials (Table 1). Because the material compositions may fluctuate, the safe limits of chemical composition were tested at laboratory scale before the pilot. It was found that lower CaO content in a CSABF clinker raw mix leads to undesirable gehlenite formation and to less ferrite formation; however, excess CaO can prevent gehlenite formation even when there is a slight fluctuation in SiO_2 and Al_2O_3 content. It is reported that the CaO content in the mix has an effect on the incorporation of iron into ye'elimite and to the formation of iron rich phases in high-iron CSA mixes [59]. The incorporation of iron to ye'elimite is increased when CaO in the mix is reduced. In this study, the low CaO mix (C3) led to a lower amount of ferrite phase and a larger amount of ye'elimite. In other mixes, the amount of ferrite was notably increased when the amount of CaO was higher.

5.2. Clinker production

Fe-slag was ground before firing, but other materials were not pretreated. The raw mix was then mixed using the Eirich mixer R11 with a volume of 250 l, which granulated the meal through a slight water addition (5 wt%); granules with 1–5 mm diameter were obtained. It was

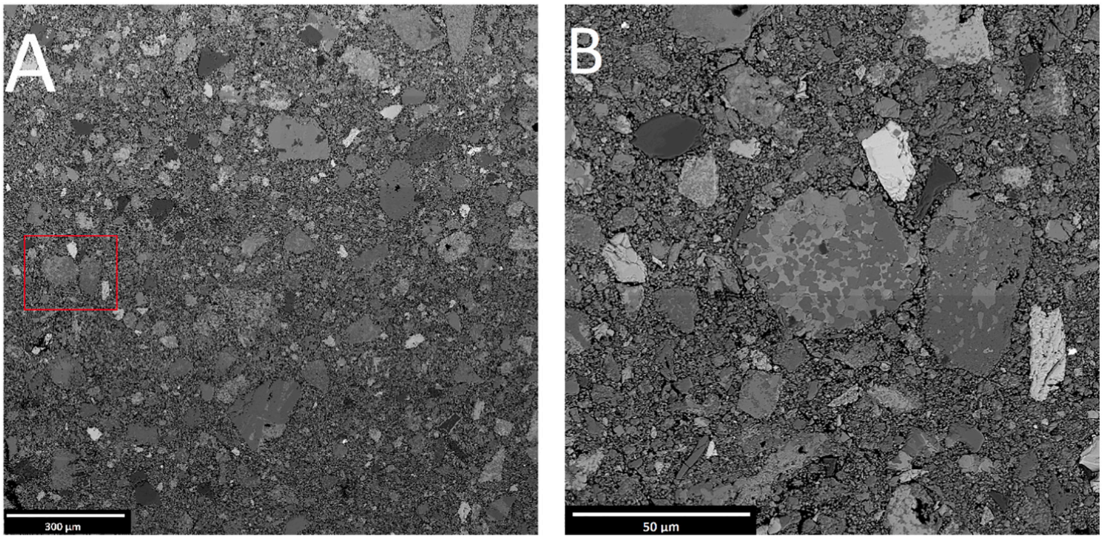

Fig. 9. SEM-BSE images from ground clinker at low (A) and higher (B) magnification. Main phases: pores/epoxy, periclase, ye'elimite, belite, ferrite, descending from darkest to lightest grey values, respectively. EDX-phase identification is shown in Fig. 10.

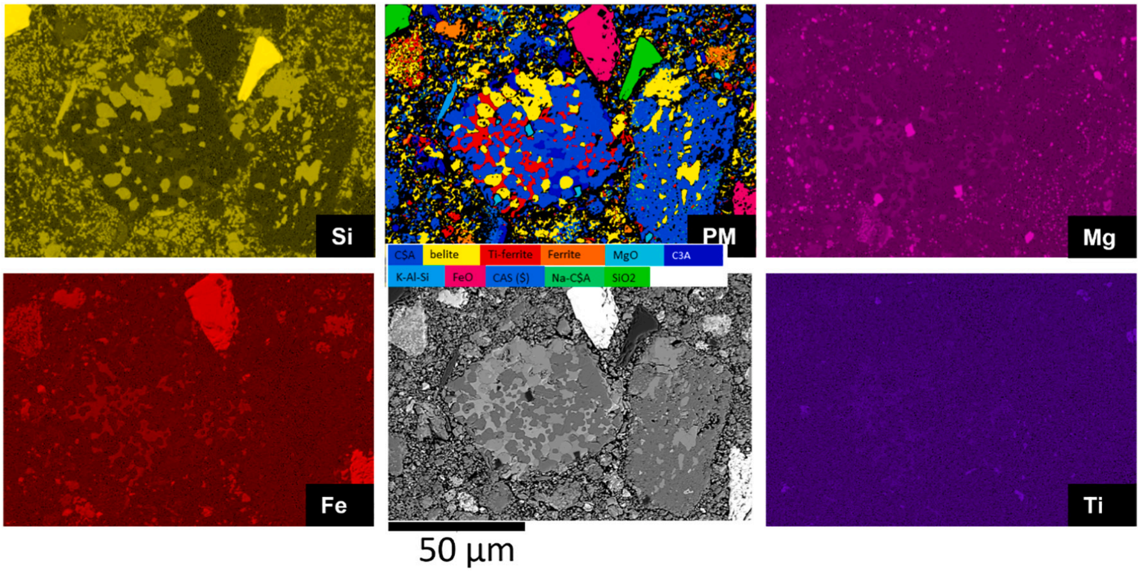

Fig. 10. Results of the EDX mapping analysis at 7 kV acceleration voltage: Elemental distribution maps were used to segment phase maps (PM) of each major phases ye'elimite, belite, Ti-ferrite, ferrite, C_3A and MgO.

observed that the granulated raw materials showed some hydration behaviour, and the granules needed to be separated manually before feeding. This is likely due to the presence of hydraulic calcium aluminates in ladle slag and in the presence of gypsum; in modern cement kilns with dry feed, this may be avoided. It must be noted that although the ladle slag had a relatively coarse particle size (~330 µm), the clinker quality was robust (see Fig. 6) throughout the trial.

Raw mix (input), kiln inlet material (20% material lost from raw meal) and clinker (output) were analysed by XRF. It was found that kiln inlet material has less iron than raw meal, and in the clinker, the iron amount was notably higher than in raw meal (Table 15). This indicates that the kiln configuration selectively increased the iron content of the final clinker, which could be due to the loss of other constituents as dust as well as to the denser nature of Fe-slag. The material loss of lighter raw materials may have been caused by high gas velocity in a relatively small kiln. During the trial, ring formation to kiln walls was observed, which is most likely caused by liquid melt formation from iron rich components.

Based on the FESEM-BSE images, it was found that the crystal size of formed clinker phases (ye'elimite, C_3A, belite, ferrite and Ti-ferrite) is - as typical for CSA clinkers – smaller than 10 µm. It has been reported that an earlier decomposition of phosphogypsum when compared to natural gypsum during firing is caused by impurities bound to phosphogypsum, which leads to decomposition at a lower temperature and a finer structure [44].

5.3. Phase composition

Based on the XRD-analysis, ye'elimite ($C_4A_3\$$) was identified to be mainly orthorhombic [39]. It is reported that orthorhombic ye'elimite can only have minor iron substitution [60,61], and the elemental substitution of aluminium by iron changes the ye'elimite structure to a pseudocubic [60] or cubic [61] structure. From the diffractogram, a clear reflection at 2-theta 18.1° that only occurred for the orthorhombic type was observed, and no signs of shifting to lower angles could be

Table 16
Average chemical composition (given in oxide wt%) of the clinker phases from EDX spot analyses (7 kV acceleration voltage using a cobalt standard for calibration) and from sum of spectra of all areas in Fig. 10 for ferrite phases.

Phase/oxide	Al_2O_3	CaO	Fe_2O_3	MgO	MnO	Na_2O	P_2O_5	SO_3	SiO_2	TiO_2
Point spectra										
Ye'elimite	49.9	35.4	0	0	0	0	0	14.6	0	0
St. deviation	0.7	0.8	0	0	0	0	0	0.7	0	0
Belite	2.4	63.3	0.8	0.0	0	0.3	0.04	3.1	30.0	0
St. deviation	0.3	0.8	1.03	0.06	0	0.14	0.1	0.6	1.1	0
Ferrite	6.5	37.25	52.59	0.77	0	0.04	0	0	2.8	0
St. deviation	1.2	1.88	2.48	0.44	0	0.09	0	0	0.8	0
Ti-Ferrite	20.31	43.82	25.99	2.76	0	0.08	0.02	0.15	1.7	5.67
St. deviation	3.84	1.21	8.31	0.95	0	0.15	0.07	0.51	0.53	6.71
C_3A	40.17	52.1	4.68	0.74	0	0.06	0	0.2	2.12	0
St. deviation	7.83	6.59	2.98	0.83	0	0.09	0	0.46	1.31	0
Sum spectra										
Na-Ye'elimite	49.03	35.28	1.88	0.12		0.28	0.99	12.38	0	0
Ferrite	7.56	36.05	48.99	1.08	0	0.1	0.00	0.60	2.95	2.66
Ti-Ferrite	21.67	39.90	23.31	2.26	4.92	0.06	0.07	1.55	1.63	4.63

Table 17
Chemical composition of Ti-ferrite and ferrite.

	Ferrite			Ti-Ferrite		
	Moles	Mole %	apfu	Moles	Mole %	apfu
Si	0.0	4.3	0.12	0.0	2.1	0.12
Ti	0.0	2.9	0.08	0.1	4.5	0.00
Al	0.1	6.5	0.37	0.2	16.3	0.33
Cr	0.0	0.0	0.00	0.0	0.0	0.00
Fe	0.3	26.9	1.53	0.1	11.2	1.68
Mn	0.0	0.0	0.00	0.1	5.3	0.00
Mg	0.0	2.3	0.07	0.1	4.3	0.05
Ca	0.6	56.3	1.60	0.7	54.7	1.70
Na	0.0	0.1	0.01	0.0	0.0	0.00
S	0.0	0.7	0.02	0.0	1.5	0.00
Total moles	1.1	100.0		1.3	100.0	
Total cations			3.8			3.9
Total O			5.0			5.0

detected at 23.7° or 41.7° [60]. These data suggest that ye'elimite has only a minor substitution of iron (Fe^{3+}) and sodium, which has been confirmed by the EDX-analysis.

Belite (C_2S) was found to be present as β-polymorph [52], which is very common in CSA-based cements due to the stabilization by minor elements [62]. γ-C_2S was not detected in the clinker, and it is unlikely to form because raw mix contains several elements that stabilise high temperature polymorphs of belite. By SEM-EDX two types of belite could be differentiated by their sulfur content. Furthermore, some of the sulfur-poor belites contain phosphorus. This reveals that the phosphorous from raw material phosphogypsum is mainly included into belite.

The ferrite content of the final clinker was slightly higher than desired due to the higher iron content of the actual clinker than originally planned. The XRD analysis showed that the ferrite phase had the best fit with the iron-rich variable of the brownmillerite-srebrodolskite series [25]. Titanium rich phase is part of the Ti -perovskovite-C_4AF mineral series.

Gehlenite, mayenite and tricalcium aluminate (C_3A) are transitory phases from raw materials, decomposition products or are stabilized by some specific impurities. They were detected by the XRD in a minor amount. The SEM-EDX did not show a needle-shaped gehlenite [62], but the EDX-analysis from a less reacted phase assemblage as shown in Fig. 12 clearly showed gehlenite together with other transitional phases.

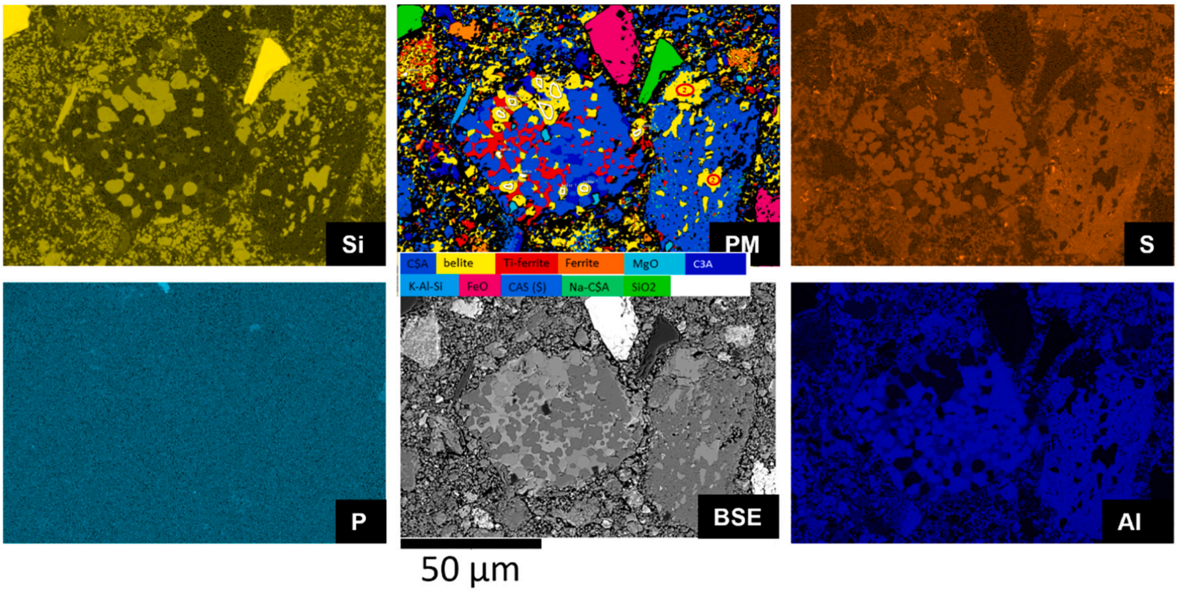

Fig. 11. SEM-EDX characterisation of belite. Phase map (PM) shows locations for spot analyses of belite-1 (white labelled areas) and belite-2 (red ellipsoids). Si and Al elemental maps confirm PM. S map indicated variation in sulfur content of belites, P map shows that single belites possess an increased P content. Results of EDX spot analyses of belites are shown in Table 18. (For interpretation of the references to colour in this figure legend, the reader is referred to the web version of this article.)

Table 18
SEM EDX spot analyses of belite-a and belite-2 and P-belite.

	Na2O	MgO	Al_2O_3	SiO_2	P_2O_5	SO_3	CaO	Fe_2O_3	CaO/SiO_2
Belite-1	0.3		2.4	30		3.1	63.3		2.1
St. deviation	0.1		0.3	1.1		0.7	0.8		
Belite-2			0.6	35.2			63.6		1.8
St. deviation				1.1			0.5		
P-belite		1.2	0.3	32.5	2.8		63.2		1.9

Tricalcium aluminate could be detected clearly with the XRD and SEM-EDX. It originates partly from ladle slag that is not completely reacted during the firing (Appendix 1 XRD of ladle slag) some of the C_3A is probably a reaction product. This is assumed because the C_3A is directly intergrown with ye'elimite, belite and other newly formed clinker phases (Fig. 10). Pure mayenite phase could not be detected by SEM-EDX. This might be because the area analysed by SEM-EDX was rather small. The limited amount of mayenite, tricalcium aluminate and gehlenite in the final clinker indicates a slight overdosage of C$ and CaO in the raw mix, which ensures the formation ye'elimite, belite and ferrite over the unwanted phases. Extra C$ seems to work as a buffer to ensure sufficient SO_x for ye'elimite formation over the formation of mayenite at 1260 °C. Sulfur is lost from anhydrite and ye'elimite as $SO_2 + O_2$, as identified in the raw mix through mass spectrometry and during the trial using a gas analyser. Sulfur loss is related to the decomposition of phosphogypsum and the decomposition of ye'elimite [44,46]. The XRF indicated that the total 2 wt% of SO_3 was lost from the raw mix during clinkering. It is noted that some of the SO_x might be lost during XRF sample preparation at 1200 °C (see Fig. 5). The lower decomposition temperature of phosphogypsum compared with natural gypsum [44] and associated sulfur loss might have caused the formation of gehlenite and mayenite over ye'elimite. The SO_x in ye'elimite might be volatilized in presence of minor elements that enhance burnability of the clinker. The decomposition of ye'elimite through the volatilization of sulfur can lead to a minor formation of mayenite [45,60], which has been reported to be common in iron-rich CSA clinkers [59,60]. Another explanation for the presence of gehlenite, tricalcium aluminate, and mayenite is that they are left as intermediate phases from the alumina source (ladle slag) that has not fully reacted during firing [3,60]. Unreacted raw materials in XRD-analysis shown in Table 13 and in Appendix 3 proves, that the reactivity of raw materials could have been improved by milling the ladle slag before firing.

5.4. Minor elements

Minor element substitution to single phases was analysed by the SEM-EDX analysis (Table 16). Ye'elimite belongs to the sodalite mineral group, which has the structure $M_4[T_6O_{12}]X$, where M presents low-charge cations (e.g. Na^+, Ca^{2+}, or Sr^{2+}), X is an anion (Cl^-, $SO_4{}^{2-}$, $WO_4{}^{2-}$ and $CrO_4{}^{2-}$) and T presents Si or Al, which occupy tetrahedral sites [39,63]. The EDX-analysis showed that most of the ye'elimite did not have a significant substitution of minor elements. However minor amounts of Na-, Fe- and S-enriched ye'elimite exists at the rim of and aggregate with transitional phases (Fig. 12). These findings indicate that maybe orthorhombic and cubic ye'elimite is present.

From the SEM-EDX presented in Table 16, the ferrite phase was calculated to be $C_2(A_{0.19},F_{0.81})$, which is close to C_6AF_2. The finding is similar to a previous study, where CSA clinkers were produced in a muffle furnace at 1300 °C from reagent-grade chemicals: from ladle slag (ferrite $C_2(A_{0.24},F_{0.76})$) [19] and phosphogypsum (ferrite ($C_2(A_{0.28},F_{0.72})$)) [20]. The ferrite phase contained traces of Si, Na, Mn, and Mg, which are typical for ferrite appearing in cements [64,65]. In previous studies, it has been found that titanium from the raw mix in CSA cements leads to the formation of perovskite (CT) [3,66,67] or that titanium

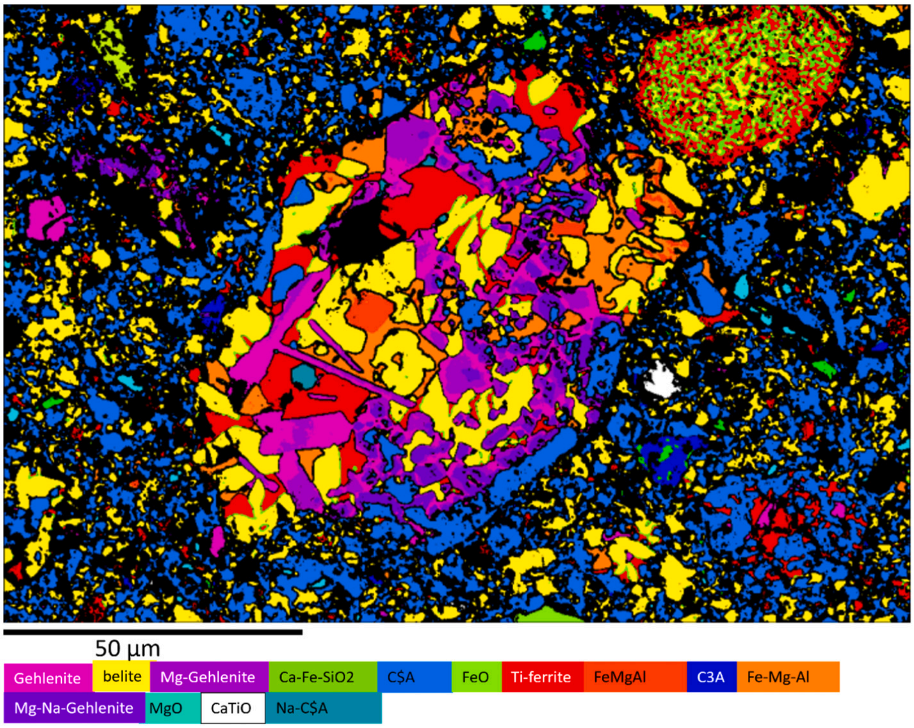

Fig. 12. Phase map from pilot clinker showing an area with transitional phases, i.e. gehlenite, Mg-rich gehlenite and also Ca-Fe-silicate.

(Ti^{4+}) can substitute iron (Fe^{3+}) in ferrite [68]. It was found through the EDX-analysis that in our study, together with ferrite (C_6AF_2), there is a titanium-rich ferrite phase present. Pure perovskite could not be identified. The formation of intermediate phases or the mixture of perovskite-brownmillerite ($CaTiO_3$–$Ca_2(Fe,Al)_2O_5$) is possible when 'the incorporation of Fe^{3+} and Al^{3+} into position of Ti^{4+} is charge balanced at the expense of oxygen vacancies (V_O) and follows the scheme $2Ti^{4+} + O^{2-} \leftrightarrow 2(Fe^{3+},Al^{3+}) + V_O$' [24].

The minor elements found in titanium-rich phase were Si, Mn, Mg, and S. The titanium from raw materials seemed to influence the formation of ferrite. The reason that an intermediate phase formed instead of pure perovskite needs to be further studied.

The impurities in belite C_2S are known to stabilise β-C_2S, α-C_2S, or α′-C_2S over γ-C_2S [62,69–72]. Al, Fe and Na found in the belite phase are common impurities from typical cement raw materials (calcite, clay, quartz, etc.), and sulfur is common in CSA clinkers. P and Na originate from industrial raw materials and are reported to effectively stabilise β-C_2S [70–72]. From the EDX-analysis, the average content of phosphorus as P_2O_5 was detected to be 0.06 wt% (i.e. close to detection limit), Na 0.3 wt% and sulfur as SO_3 3.0 wt%. But it was also shown that single belite crystals could also have much higher impurity concentrations, especially phosphorus.

The most notable impurity from the raw materials was MgO. MgO formed periclase, which is typical when there is excess MgO over the binding capacity of clinker phases [3]. Some of the MgO was bound to akermanite (C_3MS_2) and the remainder of MgO was bound to other clinker phases through elemental substitution, most notably to the ferrite phase. The possible expansion of MgO needs to be tested during durability testing. Free MgO is known to cause expansion problems in the cement when it hydrates to brucite $Mg(OH)_2$. The hydration of this MgO under a normal pressure and temperature takes a long time [73]. The expansion is especially harmful for cement if the cement is cured at elevated temperatures, which allows for a rapid reaction of periclase to brucite [50,73]. Under normal conditions, a slower rate of hydration lowers the supersaturation rate of magnesium ions around MgO crystals, which lowers the rate of brucite formation [50,73]. This means that with a slower hydration rate, Mg ions may enter the surrounding pore solution, which leads to reduced effective supersaturation, lower crystal growth pressure and stress relief in the cement paste [50,73]. One aspect of the expansion of MgO is the particle size of MgO, which was smaller in quickly cooled clinkers. The smaller particle size causes much less expansion compared to a larger particle size [73].

6. Conclusions

The industrial production of CSABF cement clinker from ladle slag, Fe-slag, and phosphogypsum has been demonstrated during a pilot-scale kiln trial. The pilot clinker was produced in a rotary kiln at 1260 °C. Even with minimal raw material homogenisation, the manufacturing process is robust, and the quality remained constant over the duration of the trial. Targeting excess CaO and C$ of a few percent over the stoichiometric calculations can ensure the formation of hydraulic clinker phases.

The chemical CO_2 emissions of pilot CSABF are 90% lower than that of OPC cement made with virgin raw materials. Due to airflow in the kiln, heavier iron bearing raw materials are concentrated in the final clinker. The total 25 wt% of the clinker is composed of minor phases that originated from raw materials, transitory phases or were formed via stabilization by the impurities from raw meal. The amorphous content of the clinker is determined to be negligible. Through SEM, it is found that the crystal size of individual phases is small (i.e. below 10 μm diameter). Some remnants from the raw materials can be detected. A minor amount of mayenite and tricalcium aluminate is formed, possibly due to the decomposition of ye'elimite and some is mostly originating from unreacted ladle slag. Iron is present in two different phases, which are part of the solid solution of the C_4AF series. The major iron-bearing phase is ferrite (C_6AF_2), and the minor phase is titanium bearing ferrite with iron/aluminium ratio close to 1. Two types of belites could be determined and high concentration of P could be found in single belite crystals. Ye'elemite has low content of minor elements.

Mg from raw materials formed periclase, which is typical when there is excess Mg over the binding capacity of the clinker phases. The highest substitution of Mg is found in ferrite as shown by SEM-EDX. The role of other impurities from raw materials to crystal formation should be further studied. Moreover, the produced clinker will be used to conduct a series of cement and concrete tests (not included here) that will be published after this work to demonstrate the mechanical, hydration, rheological, chemical and durability performance of the subsequent cement(s).

CRediT authorship contribution statement

VI: first author, conceptualization, methodology, validation, formal analysis, investigation, visualization, writing (original draft), and writing (review and editing). KO: conceptualization and writing (review and editing). TH and HKI: conceptualization, methodology, validation, and writing (review and editing). HKL and CR: conceptualization, methodology, validation, and writing (review and editing) PT: conceptualization, writing (review and editing), funding acquisition, and project administration. MI: conceptualization and writing (review and editing). TF: corresponding author, conceptualization, writing (review and editing), funding acquisition, and project administration. All authors contributed to the article and approved the submitted version.

Declaration of competing interest

There is no conflict of interest.

All the authors have approved the manuscript and agree with its submission to Cement and Concrete Research.

The CECIRE (1415/31/2015)-project was supported by Business Finland and the following companies: Boliden Harjavalta, Boliden Kokkola, Yara Suomi, Fortum Waste Solutions and Outokumpu Stainless. XRD and FESEM analysis were performed at the Center of Microscopy and Nanotechnology (University of Oulu) and F.A. Finger Institute for Building Materials Science, (Bauhaus-University Weimar)1.

The supporting companies provided permission to publish.

Acknowledgements

The work was done in the CECIRE-project, which was supported by Business Finland and the following companies: Boliden Harjavalta, Boliden Kokkola, Yara Suomi, Fortum Waste Solutions and Outokumpu Stainless. Participation of T. Hanein was funded by UKRI FLF (MR/V023829/1). The authors would like to acknowledge IBUtec and Dr. Martin Radke for setting up the pilot configuration and for technical support during the pilot study. XRD, XRF and FESEM analyses were performed at the Centre of Microscopy and Nanotechnology (University of Oulu) and F.A. Finger Institute for Building Materials Science (Bauhaus University). Simo Isokääntä from SSAB Europe Oy re acknowledged for providing ladle slag for the pilot kiln trial. We also thank Tauno Tönning Research Foundation and Walter Ahlström Foundation for the financial support of the work.

Appendix A. Supplementary data

Supplementary data to this article can be found online at https://doi.org/10.1016/j.cemconres.2022.106715.

References

[1] CEMBUREAU, activity-report-2019. https://cembureau.eu/media/clkdda45/activity-report-2019.pdf, 2019. (Accessed 25 February 2021).

[2] P. Hewlett, M. Liska, F.M. Lea, Lea's Chemistry of Cement And Concrete, 5th ed., Butterworth-Heinemann, Oxford, 2019.

[3] M. ben Haha, F. Winnefeld, A. Pisch, Advances in understanding ye'elimite-rich cements, Cem. Concr. Res. 123 (2019), 105778, https://doi.org/10.1016/j.cemconres.2019.105778.

[4] I. Galan, A. Elhoweris, T. Hanein, M.N. Bannerman, F.P. Glasser, Advances in clinkering technology of calcium sulfoaluminate cement, Adv. Cem. Res. 29 (2017) 405–417, https://doi.org/10.1680/jadcr.17.00028.

[5] T. Hanein, I. Galan, A. Elhoweris, S. Khare, S. Skalamprinos, G. Jen, M. Whittaker, M.S. Imbabi, F.P. Glasser, M.N. Bannerman, Production of belite calcium sulfoaluminate cement using sulfur as a fuel and as a source of clinker sulfur trioxide: pilot kiln trial, Adv. Cem. Res. 28 (2016) 643–653, https://doi.org/10.1680/jadcr.16.00018.

[6] I. Galan, T. Hanein, A. Elhoweris, M.N. Bannerman, F.P. Glasser, Phase compatibility in the system CaO-SiO2-Al2O3-SO3-Fe2O3 and the effect of partial pressure on the phase stability, Ind. Eng. Chem. Res. 56 (2017) 2341–2349, https://doi.org/10.1021/acs.iecr.6b03470.

[7] T. Hanein, T.Y. Duvallet, R.B. Jewell, A.E. Oberlink, T.L. Robl, Y. Zhou, F. P. Glasser, M.N. Bannerman, Alite calcium sulfoaluminate cement: chemistry and thermodynamics, Adv. Cem. Res. 31 (2019) 94–105, https://doi.org/10.1680/jadcr.18.00118.

[8] L. Zhang, M. Su, Y. Wang, Development of the use of sulfo- and ferroaluminate cements in China, Adv. Cem. Res. 11 (1999) 15–21, https://doi.org/10.1680/adcr.1999.11.1.15.

[9] E. Bescher, K. Vallens, J. Kim, Belitic calcium sulfoaluminate cement: hydration chemistry, performance, and use in the United States, in: 15th International Congress on the Chemistry of Cement Prague, 2019, pp. 16–20. https://www.researchgate.net/publication/335830876_Belitic_calcium_sulfoaluminate_cement_Hydration_chemistry_performance_and_use_in_the_United_States. (Accessed 25 February 2021).

[10] W.R. Street K.E. Roberts S. Kurlandsky , Very high early strength cement US3860433A, 1972.

[11] European Technical Assessment, ETA-19/0458, Berlin, 2020.

[12] F.P. Glasser, L. Zhang, High-performance cement matrices based on calcium sulfoaluminate-belite compositions, Cem. Concr. Res. 31 (2001) 1881–1886, https://doi.org/10.1016/S0008-8846(01)00649-4.

[13] T. Hanein, J.L. Galvez-Martos, M.N. Bannerman, Carbon footprint of calcium sulfoaluminate clinker production, J. Clean. Prod. 172 (2018) 2278–2287, https://doi.org/10.1016/j.jclepro.2017.11.183.

[14] P. Li, X. Gao, K. Wang, V.W.Y. Tam, W. Li, Hydration mechanism and early frost resistance of calcium sulfoaluminate cement concrete, Constr. Build. Mater. 239 (2020), 117862, https://doi.org/10.1016/j.conbuildmat.2019.117862.

[15] J. Kiventerä, K. Piekkari, V. Isteri, K. Ohenoja, P. Tanskanen, M. Illikainen, Solidification/stabilization of gold mine tailings using calcium sulfoaluminate-belite cement, J. Clean. Prod. 239 (2019), 118008, https://doi.org/10.1016/j.jclepro.2019.118008.

[16] K. Piekkari, K. Ohenoja, V. Isteri, P. Tanskanen, M. Illikainen, Immobilization of heavy metals, selenate, and sulfate from a hazardous industrial side stream by using calcium sulfoaluminate-belite cement, J. Clean. Prod. 258 (2020), 120560, https://doi.org/10.1016/j.jclepro.2020.120560.

[17] M. Chrysochoou, D. Dermatas, Evaluation of ettringite and hydrocalumite formation for heavy metal immobilization: literature review and experimental study, J. Hazard. Mater. 136 (2006) 20–33, https://doi.org/10.1016/j.jhazmat.2005.11.008.

[18] I. Netinger Grubeša, I. Barišić, A. Fucic, S.S. Bansode, in: Applications of steel slag in civil engineering: worldwide research, characteristics and uses of steel slag in buildingconstruction, 2016, pp. 67–82, https://doi.org/10.1016/B978-0-08-100368-8.00005-1.

[19] V. Isteri, K. Ohenoja, T. Hanein, H. Kinoshita, P. Tanskanen, M. Illikainen, T. Fabritius, Production and properties of ferrite-rich CSAB cement from metallurgical industry residues, Sci. Total Environ. 712 (2020), 136208, https://doi.org/10.1016/j.scitotenv.2019.136208.

[20] V. Isteri, K. Ohenoja, T. Hanein, P. Tankanen, H. Kinoshita, M. Illikainen, T. Fabritius, Alternative raw materials for the production of calcium sulfoaluminate cement: ladle slag and phosphogypsum, in: Proceedings of the 1st International Conference on Innovation in Low-carbon Cement & Concrete Technology, 2019.

[21] G. Belz, J. Beretka, M. Marroccoli, L. Santoro, N. Sherman, G.L. Valenti, Special Publication, in: Use of fly ash, blast furnace slag, and chemical gypsum for the synthesis of calcium sulfoaluminate-based cements 153, 1995, pp. 513–530, https://doi.org/10.14359/1086.

[22] F. Bullerjahn, M. Zajac, M. ben Haha, CSA raw mix design: effect on clinker formation and reactivity, Mater. Struct. 48 (12) (2014) 3895–3911, https://doi.org/10.1617/S11527-014-0451-Z.

[23] C.D. Popescu, M. Muntean, J.H. Sharp, Industrial trial production of low energy belite cement, Cem. Concr. Compos. 25 (2003) 689–693, https://doi.org/10.1016/S0958-9465(02)00097-5.

[24] V.v. Sharygin, E.v. Sokol, Y. Vapnik, Minerals of the pseudobinary perovskite-brownmillerite series from combustion metamorphic larnite rocks of the Hatrurim Formation (Israel), Russ. Geol. Geophys. 49 (2008) 709–726, https://doi.org/10.1016/j.rgg.2008.03.001.

[25] G.J. Redhammer, G. Tippelt, G. Roth, G. Amthauer, Structural variations in the brownmillerite series Ca2(Fe2-xAlx)O5: single-crystal X-ray diffraction at 25 °C and high-temperature X-ray powder diffraction (25 °C ≤ T ≤ 1000 °C), Am. Mineral. 89 (2004) 405–420, https://doi.org/10.2138/am-2004-2-322.

[26] K. Zhang, F. Wang, M. Rao, W. Zhang, X. Huang, Influence of ZnO-doping on the properties of high-ferrite cement clinker, Constr. Build. Mater. 224 (2019) 551–559, https://doi.org/10.1016/J.CONBUILDMAT.2019.07.075.

[27] N. Chitvoranund, F. Winnefeld, C.W. Hargis, S. Sinthupinyo, B. Lothenbach, in: Synthesis and hydration of alite-calcium sulfoaluminate cement 29, 2017, pp. 101–111, https://doi.org/10.1680/JADCR.16.00071.

[28] F. Bullerjahn, Characterisation And Hydration of Ye'elimite Containing Cements, EPFL, 2018, https://doi.org/10.5075/EPFL-THESIS-7953.

[29] S. Dolenec, K. Šter, M. Borštnar, K. Nagode, A. Ipavec, L. Žibret, Effect of the cooling regime on the mineralogy and reactivity of belite-sulfoaluminate clinkers, Minerals. 10 (2020) 910, https://doi.org/10.3390/min10100910.

[30] S. Creedy, A. Glinin, R. Matusewicz, S. Hughes, M.A. Reuter, Outotec® Ausmelt technology for treating zinc residues, in: World of Metallurgy, ERZMETALL, GDMB Informationsgesellschaft mbH, 2013, pp. 230–235. https://research.aalto.fi/en/publications/outotec-ausmelt-technology-for-treating-zinc-residues. (Accessed 25 February 2021).

[31] M. Rämä, S. Nurmi, A. Jokilaakso, L. Klemettinen, P. Taskinen, J. Salminen, Thermal processing of jarosite leach residue for a safe disposable slag and valuable metals recovery, Metals 8 (2018) 744, https://doi.org/10.3390/met8100744.

[32] H. Nguyen, V. Carvelli, E. Adesanya, P. Kinnunen, M. Illikainen, High performance cementitious composite from alkali-activated ladle slag reinforced with polypropylene fibers, Cem. Concr. Compos. 90 (2018) 150–160, https://doi.org/10.1016/j.cemconcomp.2018.03.024.

[33] H. Nguyen, E. Adesanya, K. Ohenoja, L. Kriskova, Y. Pontikes, P. Kinnunen, M. Illikainen, Byproduct-based ettringite binder – a synergy between ladle slag and gypsum, Constr. Build. Mater. 197 (2019) 143–151, https://doi.org/10.1016/j.conbuildmat.2018.11.165.

[34] K. Gijbels, H. Nguyen, P. Kinnunen, W. Schroeyers, Y. Pontikes, S. Schreurs, M. Illikainen, Feasibility of incorporating phosphogypsum in ettringite-based binder from ladle slag, J. Clean. Prod. 237 (2019), 117793, https://doi.org/10.1016/j.jclepro.2019.117793.

[35] E.D. Adesanya, A cementitious binder from high-alumina slag generated in the steelmaking process, 2019.

[36] A.M. Rashad, Phosphogypsum as a construction material, J. Clean. Prod. 166 (2017) 732–743, https://doi.org/10.1016/j.jclepro.2017.08.049.

[37] ISO 13320:2009, Particle size analysis — laser diffraction methods. https://www.iso.org/standard/44929.html, 2009. (Accessed 25 February 2021).

[38] T. Hanein, I. Galan, F.P. Glasser, S. Skalamprinos, A. Elhoweris, M.S. Imbabi, M. N. Bannerman, Stability of ternesite and the production at scale of ternesite-based clinkers, Cem. Concr. Res. 98 (2017) 91–100, https://doi.org/10.1016/j.cemconres.2017.04.010.

[39] A. Cuesta, A.G. de La Torre, E.R. Losilla, V.K. Peterson, P. Rejmak, A. Ayuela, C. Frontera, M.A.G. Aranda, Structure, atomistic simulations, and phase transition of stoichiometric yeelimite, Chem. Mater. 25 (2013) 1680–1687, https://doi.org/10.1021/cm400129z.

[40] W.G. Mumme, R.J. Hill, G. Bushnell-Wye, E.R. Segnit, Rietveld crystal structure refinements, crystal chemistry and calculated powder diffraction data for the polymorphs of dicalcium silicate and related phases, 1995.

[41] H. Morikawa, I. Minato, T. Tomita, S. Iwai, Anhydrite: a refinement, <sb:contribution><sb:title>Acta Crystallogr. Sect. B Struct. Crystallogr. Crystal</sb:title></sb:contribution><sb:host><sb:issue><sb:series><sb:title>Chem.</sb:title></sb:series></sb:issue></sb:host> 31 (1975) 2164–2165, https://doi.org/10.1107/s0567740875007145.

[42] L. Palacios, A. Cabeza, S. Bruque, S. García-Granda, M.A.G. Aranda, Structure and electrons in mayenite electrides, Inorg. Chem. 47 (2008) 2661–2667, https://doi.org/10.1021/ic7021193.

[43] M. Merlini, M. Gemmi, G. Cruciani, G. Artioli, High-temperature behaviour of melilite: in situ X-ray diffraction study of gehlenite-kermanite-na melilite solid solution, Phys. Chem. Miner. 35 (2008) 147–155, https://doi.org/10.1007/s00269-007-0206-2.

[44] Y. Shen, J. Qian, J. Chai, Y. Fan, Calcium sulphoaluminate cements made with phosphogypsum: production issues and material properties, Cem. Concr. Compos. 48 (2014) 67–74, https://doi.org/10.1016/j.cemconcomp.2014.01.009.

[45] Y. el Khessaimi, Y. el Hafiane, A. Smith, R. Trauchessec, C. Diliberto, A. Lecomte, Solid-state synthesis of pure ye'elimite, J. Eur. Ceram. Soc. 38 (2018) 3401–3411, https://doi.org/10.1016/j.jeurceramsoc.2018.03.018.

[46] F. Puertas, M.T.B. Varela, S.G. Molina, Kinetics of the thermal decomposition of C4A3S‾ in air, Cem. Concr. Res. 25 (1995) 572–580, https://doi.org/10.1016/0008-8846(95)00046-F.

[47] Y. Takéuchi, F. Nishi, Crystal-chemical characterization of the 3CaO·Al2O3—Na2O solid-solution series, Z.Kristallogr.Cryst.Mater. 152 (1980) 259–308, https://doi.org/10.1524/ZKRI.1980.152.14.259.

[48] V.G. Tsirelson, A.S. Avilov, Y.A. Abramov, E.L. Belokoneva, R. Kitaneh, D. Feil, X-ray and electron diffraction study of MgO, Acta Crystallogr. Sect. B: Struct. Sci. 54 (1998) 8–17, https://doi.org/10.1107/S0108768197008963.

[49] P. Norby, Synchrotron powder diffraction using imaging plates: crystal structure determination and rietveld refinement, J. Appl. Crystallogr. 30 (1997) 21–30, https://doi.org/10.1107/S0021889896009995.

[50] H. Kabir, R.D. Hooton, N.J. Popoff, Evaluation of cement soundness using the ASTM C151 autoclave expansion test, Cem. Concr. Res. 136 (2020), 106159, https://doi.org/10.1016/j.cemconres.2020.106159.

[51] D. Herfort, G.K. Moir, V. Johansen, F. Sorrentino, H.B. Arceo, The chemistry of Portland cement clinker, Adv. Cem. Res. 22 (2010) 187–194, https://doi.org/10.1680/adcr.2010.22.4.187.

[52] W.G. Mumme, R.J. Hill, G. Bushnell-Wye, E.R. Segnit, Rietveld crystal structure refinements, crystal chemistry and calculated powder diffraction data for the

polymorphs of dicalcium silicate and related phases, Neues Jahrb.Mineral.Abh. 169 (1995) 35–68.

[53] V.v. Sharygin, B. Lazic, T.M. Armbruster, M.N. Murashko, R. Wirth, I.O. Galuskina, E.v. Galuskin, Y. Vapnik, S.N. Britvin, A.M. Logvinova, Shulamitite Ca3TiFe3+ AlO8 - a new perovskite-related mineral from Hatrurim Basin, Israel, Eur. J. Mineral. 25 (2013) 97–111, https://doi.org/10.1127/0935-1221/2013/0025-2259.

[54] J.A. McGinnety, in: IUCr, Redetermination of the structures of potassium sulphate and potassium chromate: the effect of electrostatic crystal forces upon observed bond lengths 28, 1972, pp. 2845–2852, https://doi.org/10.1107/S0567740872007022. Urn:Issn:0567-7408.

[55] D.M. Többens, N. Stüßer, K. Knorr, H.M. Mayer, G. Lampert, E9: the new high-resolution neutron powder diffractometer at the Berlin Neutron Scattering Center, Mater. Sci. Forum 378–381 (2001) 288–293, https://doi.org/10.4028/WWW.SCIENTIFIC.NET/MSF.378-381.288.

[56] H.F. Kay, P.C. Bailey, in: IUCr, Structure and properties of CaTiO3 10, 1957, pp. 219–226, https://doi.org/10.1107/S0365110X57000675. Urn:Issn:0365-110X.

[57] B.A. Wechsler, C.T. Prewitt, Crystal structure of ilmenite (FeTiO3) at high temperature and at high pressure, Am. Mineral. 69 (1984) 176–185.

[58] P.B. Moore, T. Araki, Atomic arrangement of merwinite, Ca3Mg [SiO4] 2, an unusual dense-packed structure of geophysical interest, Am.Mineral. 57 (1972) 1355–1374.

[59] X. Yao, S. Yang, H. Dong, S. Wu, X. Liang, W. Wang, Effect of CaO content in raw material on the mineral composition of ferric-rich sulfoaluminate clinker, Constr. Build. Mater. 263 (2020), 120431, https://doi.org/10.1016/j.conbuildmat.2020.120431.

[60] F. Bullerjahn, T. Scholten, K.L. Scrivener, M. ben Haha, A. Wolter, Formation, composition and stability of ye'elimite and iron-bearing solid solutions, Cem. Concr. Res. 131 (2020), 106009, https://doi.org/10.1016/j.cemconres.2020.106009.

[61] G. Álvarez-Pinazo, A. Cuesta, M. García-Maté, I. Santacruz, E.R. Losilla, A.G.D. la Torre, L. León-Reina, M.A.G. Aranda, Rietveld quantitative phase analysis of yeelimite-containing cements, Cem. Concr. Res. 42 (2012) 960–971, https://doi.org/10.1016/j.cemconres.2012.03.018.

[62] A. Cuesta, E.R. Losilla, M.A.G. Aranda, J. Sanz, Á.G. de La Torre, Reactive belite stabilization mechanisms by boron-bearing dopants, Cem. Concr. Res. 42 (2012) 598–606, https://doi.org/10.1016/j.cemconres.2012.01.006.

[63] C.S. Hurlbut, C. Klein, Manual of mineralogy (after James D. Dana), Wiley, 1977. https://agris.fao.org/agris-search/search.do?recordID=US201300554480. (Accessed 25 February 2021).

[64] H.F.W. Taylor, Cement Chemistry, Thomas Telford Publishing, 1997, https://doi.org/10.1680/cc.25929.

[65] J. Neubauer, R. Sieber, H.J. Kuzel, M. Ecker, Investigations on introducing Si and Mg into brownmillerite - a Rietveld refinement, Cem. Concr. Res. 26 (1996) 77–82, https://doi.org/10.1016/0008-8846(95)00178-6.

[66] L. Žibret, K. Šter, M. Borštnar, M. Loncnar, S. Dolenec, The incorporation of steel slag into belite-sulfoaluminate cement clinkers, Appl. Sci. 11 (2021) 1840, https://doi.org/10.3390/app11041840.

[67] D. Koumpouri, I. Karatasios, V. Psycharis, I.G. Giannakopoulos, M.S. Katsiotis, V. Kilikoglou, Effect of clinkering conditions on phase evolution and microstructure of belite calcium-sulpho-aluminate cement clinker, Cem. Concr. Res. 147 (2021), 106529, https://doi.org/10.1016/J.CEMCONRES.2021.106529.

[68] M.B. Marinho, F.P. Glasser, Polymorphism and phase changes in the ferrite phase of cements induced by titanium substitution, Cem. Concr. Res. 14 (1984) 360–368, https://doi.org/10.1016/0008-8846(84)90054-1.

[69] M.Y. Benarchid, A. Diouri, A. Boukhari, J. Aride, J. Rogez, R. Castanet, Elaboration and thermal study of iron-phosphorus-substituted dicalcium silicate phase, Cem. Concr. Res. 34 (2004) 1873–1879, https://doi.org/10.1016/j.cemconres.2004.01.030.

[70] S. Saidani, A. Smith, Y. el Hafiane, L. ben Tahar, Role of dopants (B, P and S) on the stabilization of β-Ca2SiO4, J. Eur. Ceram. Soc. 41 (2021) 880–891, https://doi.org/10.1016/j.jeurceramsoc.2020.07.037.

[71] I. Jelenić, A. Bezjak, M. Bujan, Hydration of B2O3-stabilized α′-and β-modifications of dicalcium silicate, Cem. Concr. Res. 8 (1978) 173–180, https://doi.org/10.1016/0008-8846(78)90006-6.

[72] I.M. Pritts, K.E. Daugherty, The effect of stabilizing agents on the hydration rate of β-C2S, Cem. Concr. Res. 6 (1976) 783–795, https://doi.org/10.1016/0008-8846(76)90008-9.

[73] S. Chatterji, Mechanism of expansion of concrete due to the presence of dead-burnt CaO and MgO, Cem. Concr. Res. 25 (1995) 51–56, https://doi.org/10.1016/0008-8846(94)00111-B.